



Dislocation channel broadening A new mechanism to improve irradiation-assisted stress corrosion cracking resistance of additively manufactured 316 L stainless steel

Changing the World's Energy Future

Jingfan Yang, Laura R Hawkins, Zhongxia Shang, Evan A. McDermott, Benson Kunhung Tsai, Lingfeng He, Yu Lu, Miao Song, Haiyan Wang, Xiaoyuan Lou



DISCLAIMER

This information was prepared as an account of work sponsored by an agency of the U.S. Government. Neither the U.S. Government nor any agency thereof, nor any of their employees, makes any warranty, expressed or implied, or assumes any legal liability or responsibility for the accuracy, completeness, or usefulness, of any information, apparatus, product, or process disclosed, or represents that its use would not infringe privately owned rights. References herein to any specific commercial product, process, or service by trade name, trade mark, manufacturer, or otherwise, does not necessarily constitute or imply its endorsement, recommendation, or favoring by the U.S. Government or any agency thereof. The views and opinions of authors expressed herein do not necessarily state or reflect those of the U.S. Government or any agency thereof.

**Dislocation channel broadening A new mechanism to
improve irradiation-assisted stress corrosion cracking
resistance of additively manufactured 316 L stainless
steel**

**Jingfan Yang, Laura R Hawkins, Zhongxia Shang, Evan A. McDermott, Benson
Kunhung Tsai, Lingfeng He, Yu Lu, Miao Song, Haiyan Wang, Xiaoyuan Lou**

March 2024

**Idaho National Laboratory
Idaho Falls, Idaho 83415**

<http://www.inl.gov>

**Prepared for the
U.S. Department of Energy
Under DOE Idaho Operations Office
Contract DE-AC07-05ID14517**

Dislocation channel broadening – a new mechanism to improve irradiation-assisted stress corrosion cracking resistance of additively manufactured 316L stainless steel

Jingfan Yang^a, Laura Hawkins^{b,c}, Zhongxia Shang^d, Evan A. McDermott^e, Benson Kunhung Tsai^a, Lingfeng He^f, Yu Lu^g, Miao Song^h, Haiyan Wang^a, Xiaoyuan Lou^{a,e*}

^a School of Materials Engineering, Purdue University, West Lafayette, IN 47907, USA

^b Advanced Characterization Department, Idaho National Laboratory, ID 83402, USA

^c Department of Nuclear Engineering, College Station, Texas A&M University, TX 77843, USA

^d Electron Microscopy Center, Purdue University, West Lafayette, IN 47907, USA

^e School of Nuclear Engineering, Purdue University, West Lafayette, IN 47907, USA

^f Department of Nuclear Engineering, North Carolina State University, NC 27695, USA

^g Center for Advance Energy Studies (CAES), Idaho Falls, ID 83401, USA

^h Nuclear Engineering and Radiological Sciences, University of Michigan, Ann Arbor, MI 48109, USA

* Corresponding author. E-mail: lou49@purdue.edu (X. Lou).

Abstract

Additively manufactured (AM) 316L stainless steel (SS) after hot isostatic pressing (HIP) was found to exhibit superior resistance to irradiation-assisted stress corrosion cracking (IASCC) in high-temperature water, as compared to wrought 316L SS. The well-accepted IASCC factors of radiation-induced segregation (RIS) and radiation hardening are not accurate descriptions of IASCC susceptibility in this case. A decreased strain localization along grain boundaries, caused by dislocation channel broadening, was confirmed to suppress crack initiation. A unique distribution of irradiation-induced defects in HIP AM 316L SS eased dislocation cross-slip compared to those in the wrought counterpart, thus increasing the channel width near the grain boundaries. For the first time, this study highlights the importance of dislocation channel broadening as a potential mechanism to further improve the IASCC resistance of 316L SS and provides direct experimental evidence based on commercial-grade materials.

Keywords: 316L stainless steel, additive manufacturing, irradiation-assisted stress corrosion cracking (IASCC), dislocation channel broadening, grain boundary

1. Introduction

Additive manufacturing (AM) is being evaluated by the nuclear industry to support future reactor component manufacturing and revolutionize reactor service. This manufacturing method offers the potential to shorten the supply chain, enable unparalleled design flexibility, and accelerate the deployment schedule. In the past few years, extensive research has been conducted specifically looking into the performance of AM 316L stainless steel (SS) in nuclear environments, including microstructural features [1–3], mechanical properties [4,5], radiation damages [6,7], corrosion [8], stress corrosion cracking (SCC) [9,10], and irradiation-assisted stress corrosion cracking (IASCC) [11–13].

Song et al. [11] reported the excellent IASCC resistance of AM 316L SS made by laser powder bed fusion (LPBF) AM in high-temperature water when hot isostatic pressing (HIP) was applied. Under the same testing conditions, AM 316L SS was found immune to IASCC when its wrought counterpart exhibited extensive cracking. The U.S. Nuclear Regulatory Commission (NRC) soon highlighted this phenomenological observation and emphasized the importance of understanding AM materials' nuclear-specific properties and the effects of post-AM processing [14]. Literature data concerning the radiation effects on AM materials have been increasing over the years. Discrepancies exist in almost all the studied areas [7,11,13,15]. Note that most of these studies mainly reported the observations, with little mechanistic insight to explain the differences between AM and conventional materials, which is critical to regulating AM for long-term nuclear service. Microstructural variation is generally considered the main reason behind all these conflicting conclusions. Radiation effects were highly dependent on local microstructure and microchemistry. Understanding the underlying mechanisms behind these observations provides the regulatory basis for qualifying AM materials for nuclear use and assessing long-term risks.

Austenitic 316L SS, widely used for manufacturing in-core components, was found susceptible to IASCC in high-temperature water [2,18,19]. IASCC involves multiple factors, including stress, corrosion, and radiation, making it challenging to identify the dominant mechanism. Earlier work suggested that radiation-induced segregation (RIS) on grain boundaries (GBs) and radiation hardening are the primary factors, while later studies confirmed that neither could necessarily lead to IASCC [16–19]. Localized deformation along grain boundaries was recently recognized as contributing to IASCC cracking initiation. It is believed that the stress localization on GBs through dislocation channel-GB interaction would facilitate microcrack initiation [20–22]. 316L SS

exhibited Cr depletion on GBs after radiation [23]. Stress localization on GBs is elevated by radiation hardening, and can rupture the surface oxide film and expose GBs directly to the corrosive environment, accelerating the dissolution and promoting IASCC [24].

Dislocation channeling originates from the constrained plastic flow during the deformation of irradiated alloys. It is associated with the interaction between dislocation and radiation induced defects such as voids, loops, and stacking fault tetrahedra (SFTs). The defects could be partially or fully cleared in channels through the defect absorption mechanisms [25] or the defect annihilation mechanisms [26], resulting in the preferential glide within the channels for the subsequent dislocations. Multiple factors were found to contribute to dislocation channeling, including stacking fault energy (SFE), irradiation dose, temperature, strain rate, and the types and density of radiation-induced defects [27–29]. The deformation degree of dislocation channeling can be quantified by the spacing between channels, channel height, and channel width. Previous studies [13,30–32] believed that the channel height is essential as it is proportional to the number of dislocations accumulated in the channel. Channel width is usually treated as a constant value, ~100 nm. However, extensive experimental and modeling studies [33–36] revealed that dislocation channel width could vary from tens of nanometers to hundreds of nanometers, suggesting that the contribution of channel width to strain localization should not be negligible. Still, the connection between channel width and IASCC behavior has not yet been demonstrated by either experimental observation or simulation.

In the present work, we investigated the origin of the superior IASCC resistance of HIP AM 316L SS reported by *Song et al.* [11] as compared to wrought AM 316L SS. The effects of multiple factors on IASCC were systematically explored, including alloy composition, grain structure, RIS, radiation hardening, radiation-induced defects, and channel density/height, none of which provides a direct explanation. A comprehensive characterization of dislocation channels along with the local strain analysis revealed channel broadening in HIP AM 316L SS is the leading mechanism that lowered the strain localization along the GBs, and therefore reduced the chance of IASCC initiation. The potential mechanisms that induced channel broadening in HIP AM 316L SS as compared to its wrought counterpart are also discussed.

2. Experimental

2.1. Materials and heat treatment

The commercial 316L SS powder was provided by Carpenter Powder Products (Bridgeville, PA, USA), with a mesh size from -100 to +325 (~45-100 μm). AM 316L SS blocks were printed by an EOS M270 LPBF AM system at Quad City Manufacturing Laboratory (Rock Island, IL, USA). Printing parameters of 195 W laser power, 1200 mm/s scan speed, and 20 μm layer thickness were applied to achieve good material density. The HIP treatment of 1150 $^{\circ}\text{C}$ for 4 hours and 1000 bar was performed in argon, and followed by solution annealing (SA) at 1066 $^{\circ}\text{C}$ for 1 hour and water quenching to minimize the potential sensitization caused by the slow cooling process of HIP.

The wrought 316L SS used in this study was initially ordered by GE-Hitachi Nuclear Energy from Crucible Specialty Metals. The material was further annealed at 1066 $^{\circ}\text{C}$ for 50 min, followed by water quenching. The chemical compositions of the HIP AM 316L SS and wrought 316L SS are listed in Table 1.

Table 1. Chemical compositions of HIP AM 316L SS and wrought 316L SS were measured by inductively coupled plasma–optical emission spectrometry (ICP-OES).

Element (wt.%)	Fe	Cr	Ni	Si	Mn	Mo	Co	C	N	O
HIP AM 316L SS	Bal.	16.9	10.7	0.71	1.13	2.24	0.12	0.027	0.094	0.0384
Wrought 316L SS	Bal.	16.2	10.1	0.35	1.59	2.06	0.17	0.017	0.085	-

2.2. Proton irradiation

HIP AM and wrought 316L SS were machined to two types of geometry: tensile bar and TEM bar. The tensile bar was designed for the IASCC initiation test with a square cross-section of 2 mm by 2 mm and a gauge length of 21 mm. The geometry of the tensile bar was described in detail in our previous work [23] and elsewhere [13,30]. The TEM bar is 20 mm long with a square cross-section of 2 mm by 2 mm. Fig. 1(a) shows the schematic of tensile and TEM bars relative to the build direction and load direction for HIP AM 316L SS. The tensile specimen was machined with crack initiation along the build direction (loading along the Y direction). For AM 316L SS, it has been concluded that this direction presents the highest cracking susceptibility in AM 316L SS

[11,37]. The TEM bar was extracted from the AM block in the same manner (Fig. 1(a)). The gauge section of the tensile bars and the TEM bars were first ground from 120 grits to 800 grits by SiC paper and then electropolished with 10 vol% perchloric acid of methanol solution at 40 V for 30 sec to achieve a scratch-free surface.

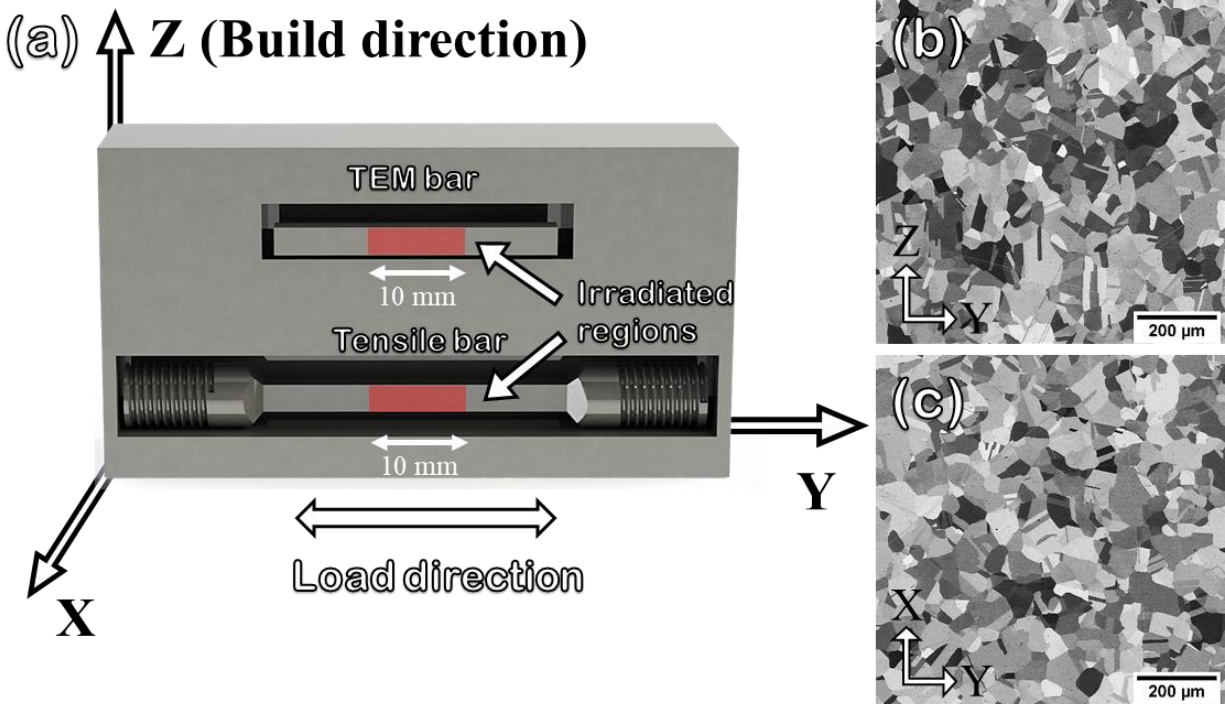


Fig. 1. (a) Drawing of the tensile and TEM bars relative to the build direction and load direction for HIP AM 316L SS. The proton radiation was conducted on the Z-Y plane (as is highlighted with the red color), and the load was applied along the Y direction; (b) SEM backscattered electron image showing the grain structure of HIP AM 316L SS from the Z-Y plane; (c) SEM backscattered electron image showing the grain structure of HIP AM 316L SS from the X-Y plane.

Proton irradiation was conducted on the well-polished surface of these specimens by a 3 MV National Electronics Corporation Pelletron accelerator in Michigan Ion Beam Laboratory (MIBL) at the University of Michigan. A total of 2 MeV protons with the fluence of $\sim 7 \times 10^{19}$ ions/cm² were performed within a 2 mm by 10 mm area in the center of the specimens at 360 °C, resulting in a damage level of 2.5 dpa at 10 μm below the surface. The radiation depth profile was estimated based on the Kinchin-Pease (K-P) mode in Stopping and Range of Ions in Matter (SRIM) [38] simulation, and the total penetration depth was ~ 20 μm. A flux of 1.9×10^{14} - 2.4×10^{14} ions/cm²s was delivered during the test, corresponding to a damage rate of 6.9×10^{-6} - 8.7×10^{-6} dpa/s.

2.3. Microhardness

Radiation hardening was evaluated by measuring the hardness before and after proton irradiation, using a MICROMET II Vickers hardness indenter. A total of 25 indents were made on each specimen to get statistically meaningful results. A load of 25 gf with 15 sec dwell time was applied for each indent, providing a plastic deformation zone within the irradiated depth (<20 μm below the surface), as shown elsewhere [12].

2.4. Constant extension rate tensile (CERT) test

The CERT test was used to evaluate the IASCC susceptibility of HIP AM and wrought 316L SS specimens after proton irradiation. The test was conducted in a simulated boiling water reactor (BWR) normal water chemistry (NWC) environment (288 °C, 1500 psi, 2 ppm dissolved oxygen, 20 ppb sulfate) with a strain rate of $1 \times 10^{-7} \text{ s}^{-1}$. The details of the testing apparatus were described elsewhere [9]. The specimens were pulled to 4% and 6% plastic strain to get representative IASCC behaviors. 20 ppb sulfate injection has been standardized for accelerating the cracking severity in the BWR-NWC environment without altering the cracking mode [39,40].

2.5. Microstructure, dislocation channel, and crack characterization

HIP AM and wrought 316L SS samples for microstructure characterization were prepared using a PACE NANO-2000S auto polisher. The samples were first ground with a 320 grit SiC pad and then polished with 9 μm , 3 μm , and 0.05 μm diamond suspension until a scratch-free surface was achieved. The sample preparation was completed by vibratory polishing with 0.03 μm colloidal silica suspension in a PACE GIGA900 vibratory polisher.

Scanning electron microscope (SEM) and electron backscatter diffraction (EBSD) characterization were performed by using an FEI Quanta 650 SEM equipped with an EDAX EBSD detector. The dislocation channels and cracks after the CERT tests were characterized at 10 kV with a working distance of 10 mm. EBSD scans were applied in a rectangle zone of 811 $\mu\text{m} \times 634 \mu\text{m}$ at 20 kV and 1.7 μm step size. EBSD was also conducted on the IASCC samples after the CERT tests to select the comparable grains with a similar crystallographic orientation for transmission electron microscopy (TEM) characterization. To ensure imaging quality, the surface oxides were stripped off by using two types of solutions: sodium hydroxide (10%) and potassium permanganate (30%) in DI water, and ammonium oxalate (10%) in DI water. The EBSD data was

processed by using the MTEX toolbox in MATLAB to obtain the grain orientations, grain boundary mappings, Schmid factors, and slip vectors.

TEM lamellae of HIP AM and wrought 316L SS after CERT tests were fabricated by focused ion beam (FIB) lift-out technique using an FEI Quanta 3D FEG dual beam SEM at the Center for Advanced Energy Studies (CAES). A platinum overlay was first deposited in the area of interest to prevent the sample from ion damage. These lamellae were then carefully thinned step-by-step until ~100 nm using ion milling under low voltage (2 keV). Most of the TEM work was done in an FEI Talos F200X FEG STEM at Idaho National Laboratory, including channel morphology characterization and STEM-EDX analysis. A voltage of 200 kV was applied for both TEM and STEM modes. Thermo Scientific Velox software was used to analyze the STEM-EDX data. The aberration-corrected high-resolution TEM characterization of dislocation channels was carried out by a Thermo Scientific Themis Z S/TEM at 300 kV accelerating voltage at the Electron Microscopy Center at Purdue University.

2.6. Atomic force microscopy (AFM)

The height and width of dislocation channels were measured by a Bruker Dimension Icon AFM. Before the probe scanning, SEM and EBSD were taken in an area of ~1200 μm by 700 μm from the irradiated region of the strained IASCC specimens to document the dislocation channel morphology, grain orientation, grain boundary type, and Schmid factor for the grains. Then AFM characterization was conducted on the selected grains. The selection criteria for these grains will be discussed in detail in the discussion section. The AFM image was taken under Scanasyt mode using a Bruker SCANASYST-AIR tip. A high-resolution scanning was achieved with a 0.5 Hz scan rate and 512 sample/line. After the scanning, the AFM files were loaded to ProfimOnline software and the dislocation channel width and height were obtained by conducting the line measurements perpendicular to the dislocation channels.

2.7. Modeling of dislocation channel broadening

The effect of radiation induced defects on channel broadening was simulated based on a stochastic model adapted from *Doyle et al.* [33]. The model assumes the average dislocation interaction distance along the glide plane as ΔL , which is associated with the defect density (N)

and size (d). That is, $\Delta L = (Nd)^{-0.5}$. Each time a dislocation interacts with a defect, it will stochastically jog up or down with a distance of $d/2$ and eliminate the defect from the interaction matrix. Dislocations were emitted at a fixed point, one at a time, from one side of the defect matrix. To get a representative channeling behavior, each condition with a given defect size and density included 1000 histories, each containing 500 dislocations. As a result, the channel width at a certain propagation distance can be determined as the distance between the highest and lowest glide planes. The details regarding this model can be found in the reference [33]. In this study, the channel width was collected at 50 μm away from the source, which is close to the average grain size of HIP AM and wrought 316L SS. Defect sizes from 1 nm to 35 nm with 5 nm space and densities from 1.1 ($10^{21}/\text{m}^3$) to 20 ($10^{21}/\text{m}^3$) with a space of 5 ($10^{21}/\text{m}^3$) were calculated.

3. Results

3.1. Microstructure of HIP AM and wrought 316L SS

Although AM 316L SS by LPBF AM under as-built state usually present highly textured microstructure [10], it is not uncommon that high-temperature heat treatment can promote complete recrystallization and produce equiaxed coarse grain structure with random texture, benefiting from its higher residual strain after processing. In this case, after HIP+SA, the material was found isotropic in all directions (Figs. 1(b) and (c)), similar to the fully-annealed wrought 316L SS. In fact, our previous study [37] reported comparable tensile behavior of HIP AM 316L SS tested from the Y and Z directions, suggesting the isotropic mechanical property. Isotropic microstructure and mechanical behavior of AM 316L SS after high-temperature treatment were also reported elsewhere [41–43]. In Figs. 2(a) and (b), HIP AM 316L SS exhibited an equiaxed grain structure from the Z-Y plane with a grain size of $51.9 \pm 39.1 \mu\text{m}$, similar to the wrought counterpart with a grain size of $54.8 \pm 39.7 \mu\text{m}$ (Figs. 2(e) and (f)). The length fraction of twin boundary (CSL3) in the HIP AM and wrought 316L SS is 48.8% and 46.8%, respectively. Both materials show random texture (Figs. 2(c) and (g)). A larger area ($\sim 1.3 \text{ mm}^2$) of the EBSD scan was also included in Supplementary Fig. S1, confirming the equiaxed grain structure with random texture in HIP AM 316L SS.

Fig. 2(d) shows a TEM bright field image of HIP AM 316L SS, confirming that the high-temperature treatment completely removed the cellular dislocation structures produced by AM, as comparable to wrought 316L SS (Fig. 2(h)). A small amount of oxide particles was present along

the grain boundaries of HIP AM 316L SS (Fig.2(d)), resulting from the oxygen content from SS feedstock powders and oxide coarsening, both of which have been extensively reported [44]. The oxides were further confirmed as Si-Mn rich oxides by STEM-EDX, as shown in Supplementary Fig. S2.

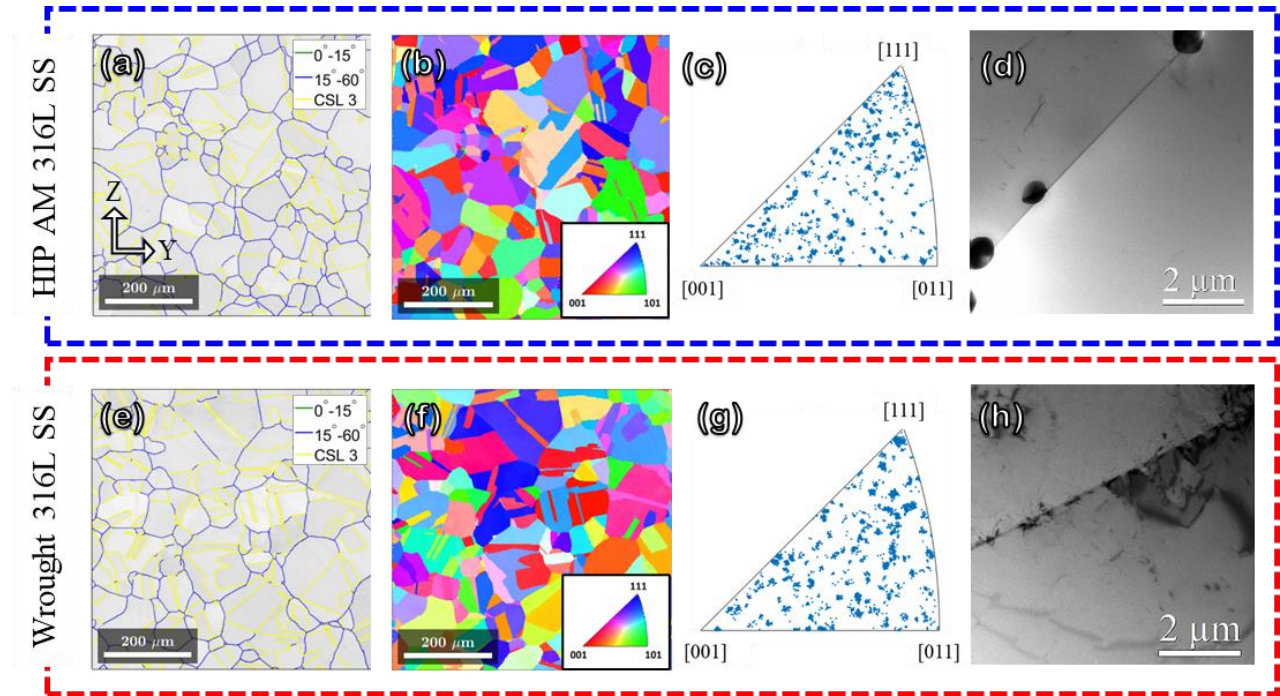


Fig. 2. Microstructure characterization of HIP AM and wrought 316L SS without irradiation. (a)-(d) are the EBSD boundary mapping, EBSD IPF mapping, EBSD grain orientation distribution mapping, and bright-field TEM image of the HIP AM 316L SS, respectively. (e)-(h) are the figures of the wrought 316L SS with the same types. The comparison suggests a similar microstructure between the HIP AM 316L SS and the wrought 316L SS.

3.2. IASCC evaluation

Fig. 3(a) compares the IASCC susceptibility of HIP AM and wrought 316L SS after the 4% and 6% CERT test in high-temperature water, respectively. The 4% data was referred from our previous study [11]. No crack was observed from HIP AM 316L SS in both testing conditions, while extensive intergranular cracking appeared in wrought 316L SS, suggesting the HIP AM 316L SS showed excellent IASCC resistance in high-temperature water. Intergranular cracks in the irradiated region of wrought 316L SS are primarily perpendicular to the load direction, as shown in Fig. 3(b). A similar IASCC cracking behavior of wrought 316L SS was also reported

elsewhere [13,45]. Extensive dislocation channeling was present in both HIP AM and wrought 316L SS (Fig. 3(c)).

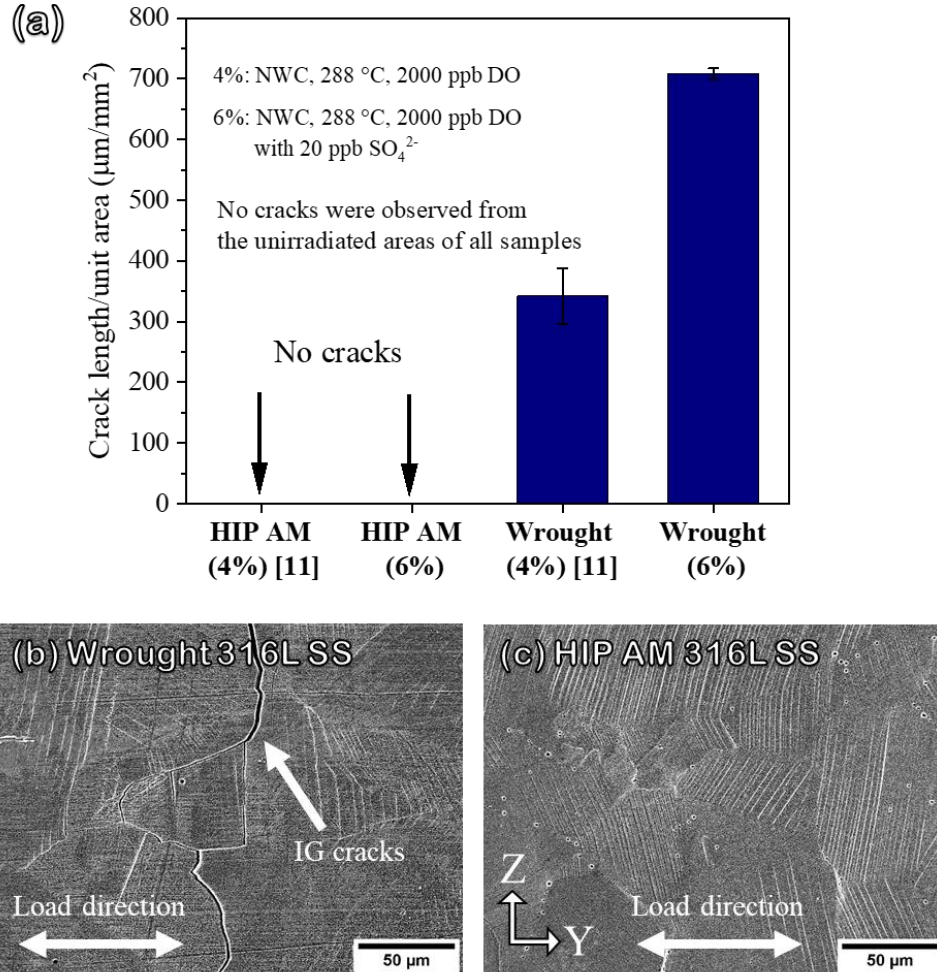


Fig. 3. (a) IASCC crack density of the HIP AM and wrought 316L SS after 4% [11] and 6% of CERT tests. No cracks were observed from the HIP AM 316L SS sample; (b) SEM image shows the intergranular cracks in the wrought 316L SS sample after 6% of the CERT test. (c) SEM image shows the sample surface of HIP AM 316L SS after 6% of the CERT test.

3.3. Proton radiation effect on HIP AM and wrought 316L SS

3.3.1. Radiation induced segregation (RIS)

RIS in terms of Fe, Cr, Ni, and Si segregation on the grain boundaries of HIP AM and wrought 316L SS after 2.5 dpa proton irradiation is shown in Fig. 4. Fe, Cr depletion, and Ni, Si enrichment were measured from the grain boundaries of both materials, consistent with the typical RIS of

316L SS reported by other studies [46,47]. The grain boundaries in the HIP AM 316L contained ~2 wt.% less Fe (Fig. 4(a)) and ~4 wt.% less Ni (Fig. 4(c)) than those in the wrought counterpart. In Fig. 4(b), a similar degree of Cr depletion was found in both materials on grain boundaries (11.5 wt.% for HIP AM 316L SS vs. 11.7 wt.% for wrought 316L SS). More Si was segregated on grain boundaries in HIP AM 316L SS (3.7 wt.% vs. 2.1 wt.%). Si was believed to promote intergranular IASCC [48] and stress corrosion cracking [49,50] due to the dissolution of Si-rich oxide in high-temperature water. Other minor elements not presented in the figures are either because they are less reactive with oxygen, such as P [48], or their roles in SCC are unclear. In general, the differences in RIS between the two materials are insignificant. It is highly unlikely that the present differences in GB segregations could be a key contributor to the IASCC difference reported in the earlier section.

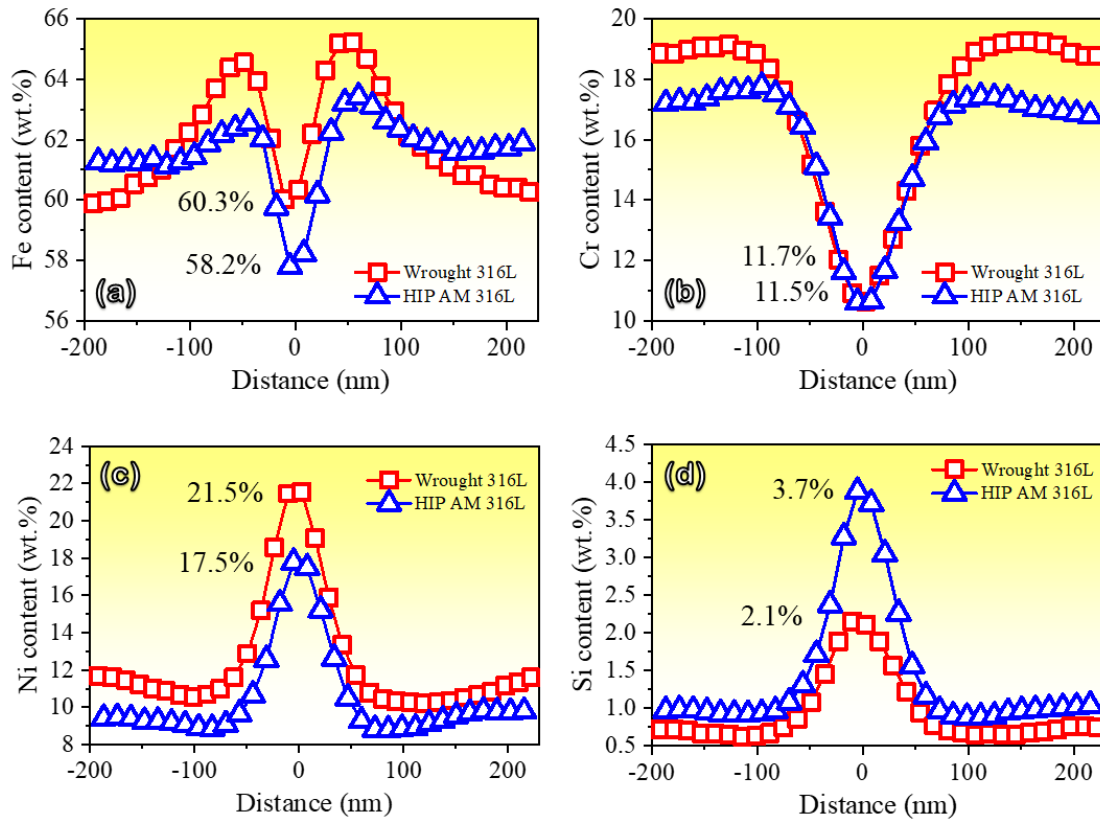


Fig. 4. Radiation-induced segregation (RIS) in terms of (a) Fe, (b) Cr, (c) Ni, and (d) Si distribution on grain boundaries of HIP AM and wrought 316L SS after 2.5 dpa proton irradiation at 360 °C.

3.3.2. Radiation hardening and radiation damage

Radiation hardening of HIP AM and wrought 316L SS, demonstrated by hardness change, is shown in Fig. 5. Before radiation, the two materials exhibited similar hardness values. The hardness after radiation for HIP AM 316L SS is $417 \pm 14 \text{ kg/mm}^2$, which is ~30% higher than the wrought counterpart ($322 \pm 29 \text{ kg/mm}^2$).

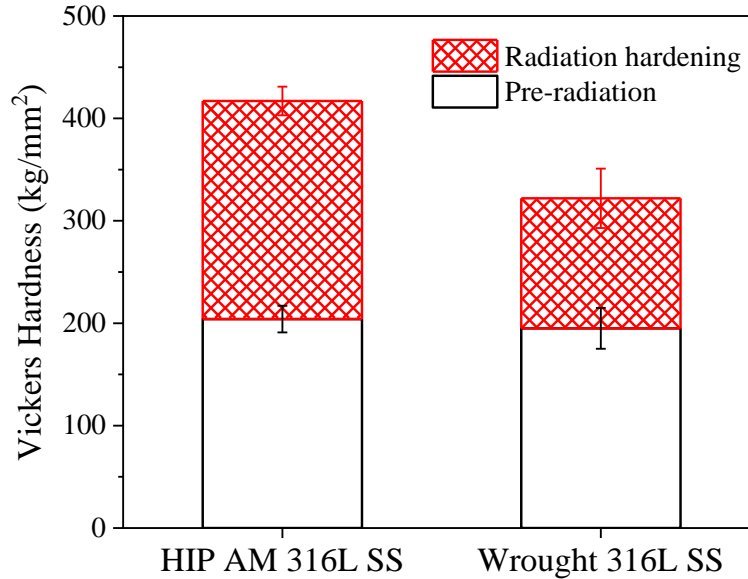


Fig. 5. Radiation hardening of HIP AM and wrought 316L SS after 2.5 dpa proton radiation at 360 °C. The white columns at the bottom represent the hardness without radiation. The red columns on the top are the radiation hardening.

Radiation hardening stems from radiation induced damages, primarily voids and dislocation loops for 316L SS. The dispersed barrier hardening (DBH) model [51] was utilized to calculate the contribution of these features to radiation hardening. The equation is listed in Eq. 1.

$$\Delta\sigma = M\alpha\mu b(Nd)^{0.5} \quad \text{Eq. 1}$$

$\Delta\sigma$ (MPa) is the change of yield strength contributed by obstacles, M is the Taylor factor (3.06), α is the strength factor, μ is the matrix shear modulus (77.47 GPa), b is the Burgers vector of the material (0.253 nm), N is the number density of the obstacles, and d is the size of the obstacles. The measurement of voids and dislocation loops used in the calculation here were referred from our previous work [11]. The results are listed in Table 2. It is not surprising that dislocation loops dominated hardening in both materials as they are strong barriers to dislocations. The DBH model reasonably predicted the hardness increase as a combined effect of voids and dislocation loops in

both materials, confirming that the higher hardness measured from HIP AM 316L SS originated from the defects. Although radiation hardening is recognized as a critical factor for IASCC [18,52], the mechanism does not explain the higher IASCC resistance of HIP AM 316L SS. The more severe radiation hardening in HIP AM 316L SS contradicts its excellent IASCC resistance.

Table 2. The contribution of voids and dislocation loops on radiation hardening of HIP AM and wrought 316L SS was calculated by the Dispersed Barrier Hardening (DBH) model.

	HIP AM 316L SS	Wrought 316L SS
Void size (nm)	8.4	19.5
Void density ($10^{21}/\text{m}^3$)	0.08	0.34
Swelling (%)	0.0025	0.156
Loop size (nm)	20.2	32.6
Loop density ($10^{21}/\text{m}^3$)	15	3.2
$\Delta H_{\text{v Loop}}$ (HV)	194.3	130.3
$\Delta H_{\text{v Void}}$ (HV)	13.3	58.8
$\Delta H_{\text{V, microstructure}}$ (HV)	196.30	146.05
$\Delta H_{\text{V, measured}}$ (HV)	213	127

3.4. Dislocation channels

Dislocation channel spacing and height are widely used to quantify the degree of localized deformation. The channel spacing and height in HIP AM and wrought 316L SS were characterized by SEM and AFM after 6% CERT test. The data was collected from 90 channels in 25 grains from each material. As illustrated in Supplementary Fig. S3, channel spacing refers to the average distance between two neighboring dislocation channels, and channel height is the out-of-plane displacement induced by dislocations. In Fig. 6, the channel spacing is similar in both conditions at $2.86 \pm 0.63 \mu\text{m}$ for HIP AM 316L SS and $2.78 \pm 0.93 \mu\text{m}$ for wrought 316L SS. Weighted average channel height is employed to represent the channel height, as a larger height usually suggests greater susceptibility to crack initiation [20,30]. It can be calculated based on Eq. 2, where h_i is the channel height for the i th channel.

$$\bar{h} = \frac{\sum_{i=1}^n h_i^2}{\sum_{i=1}^n h_i} \quad \text{Eq. 2}$$

As shown in Fig. 6, the weighted average channel height in HIP AM 316L SS is 290.8 nm, significantly smaller than in wrought 316L SS (361.9 nm). The height of the dislocation channel is believed to reflect the number of dislocations within the channel since each dislocation glide is equivalent to its Burgers vector [30]. The smaller channel height in HIP AM 316L SS may suggest a reduced strain localization on GBs, revealing a consistent trend in IASCC susceptibility of the two materials.

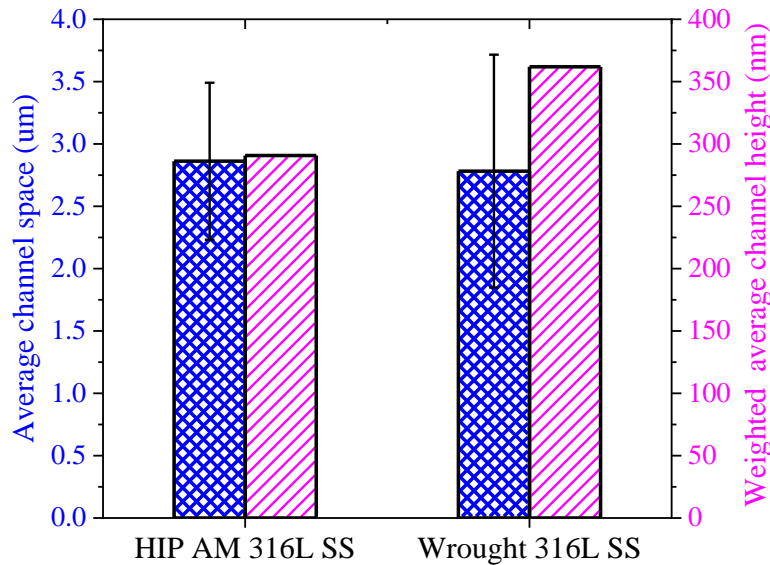


Fig. 6. Dislocation channel characterizations of HIP AM and wrought 316L SS after 6% of CERT test in high-temperature water, including average channel space (the blue columns) and weighted average channel height (the pink columns).

4. Discussion

Above, we compared the steel composition, microstructure, RIS, and radiation hardening of HIP AM and wrought 316L SS, none of which provided direct evidence to support the high IASCC resistance of HIP AM 316L SS. HIP AM 316L SS contained slightly more Si and O, resulting in a higher density of Si-Mn rich oxides. Si-rich oxides are somewhat soluble in high-temperature water (unlike Fe, Ni, and Cr oxides) [3,50,53], which was believed to increase cracking susceptibility in stainless steels. Other impurities, such as N and P, were reported to have minor effects on SCC in high-temperature water [54,55]. The most notable difference is in dislocation

channel morphology, suggesting strain localization is different between the two materials. An in-depth discussion on channel formation will be provided in the following sections.

4.1. Dislocation channeling in HIP AM and wrought 316L SS

4.1.1. The selection criteria for dislocation channel study

TEM lamellae were prepared by FIB, lifting out a series of dislocation channels from selected grains in HIP AM and wrought 316L SS specimens after 6% CERT test. Selection criteria were established to achieve a fair comparison of channels between the two materials.

First, the dislocation channels should terminate at the grain boundaries instead of transmitting through, which ensures a similar GB-dislocation channel interaction, as shown in Figs. 7(a) and (b). This arrangement implies a relatively high stress/strain localization [20,32]. Second, the Schmid factors of the two grains need to be similar (Table 3), corresponding to a similar shear stress applied to the slip plane. Third, the grain orientation, as well as the grain boundary misorientation angle, were also similar. Figs. 7(c), (d), (e), and (f) confirmed that the crystallographic orientation of the two selected grains is close to $\langle 111 \rangle$. The Euler angles of the grains are presented in Table 3. While it is challenging to locate grain boundaries that shared similar grain misorientation angles and also satisfied other criteria, the studied GBs were both high-angle GBs (Figs. 7(e) and (f)). Several studies reported the promise of using geometric compatibility factor, m' , to predict slip resistance across a GB [56,57]. The m' can be expressed as

$$m' = \cos \psi \cdot \cos \kappa \quad \text{Eq. 3}$$

where ψ is the angle between the normal directions of two slip planes (target grain and its neighboring grain), and κ is the angle between the slip directions. The geometrical description of m' is shown in Fig. S4 in the supplementary document. $m' = 1$ refers to the GB being transparent to dislocation slip, and $m' = 0$ means an impenetrable GB. *Guo et al.* [58] found that an impenetrable GB typically has m' less than 0.5. The calculated m' for all the TEM samples in this study were less than 0.5 (Table 3), suggesting a high resistance to dislocation slip. In this work, two representative TEM samples were studied based on the same selection criteria for each material. The details of the grain parameters are listed in Table 3.

Table 3. Schmid factor, grain orientation, grain boundary angle, and geometric compatibility factor of two comparable grains in the HIP AM and wrought 316L SS.

		Schmid factor	Grain orientation $\langle \phi_1, \Phi, \phi_2 \rangle$ in ($^\circ$)	Grain boundary angle ($^\circ$)	m'
Group 1	HIP AM	0.4342	$\langle 233.0, 124.4, 328.1 \rangle$	48.9	0.36
	Wrought	0.4304	$\langle 153.6, 129.3, 214.4 \rangle$	36.4	0.11
Group 2	HIP AM	0.3051	$\langle 93.4, 146.9, 226.0 \rangle$	20.4	0.02
	Wrought	0.3907	$\langle 40.9, 123.2, 326.4 \rangle$	49.8	0.12

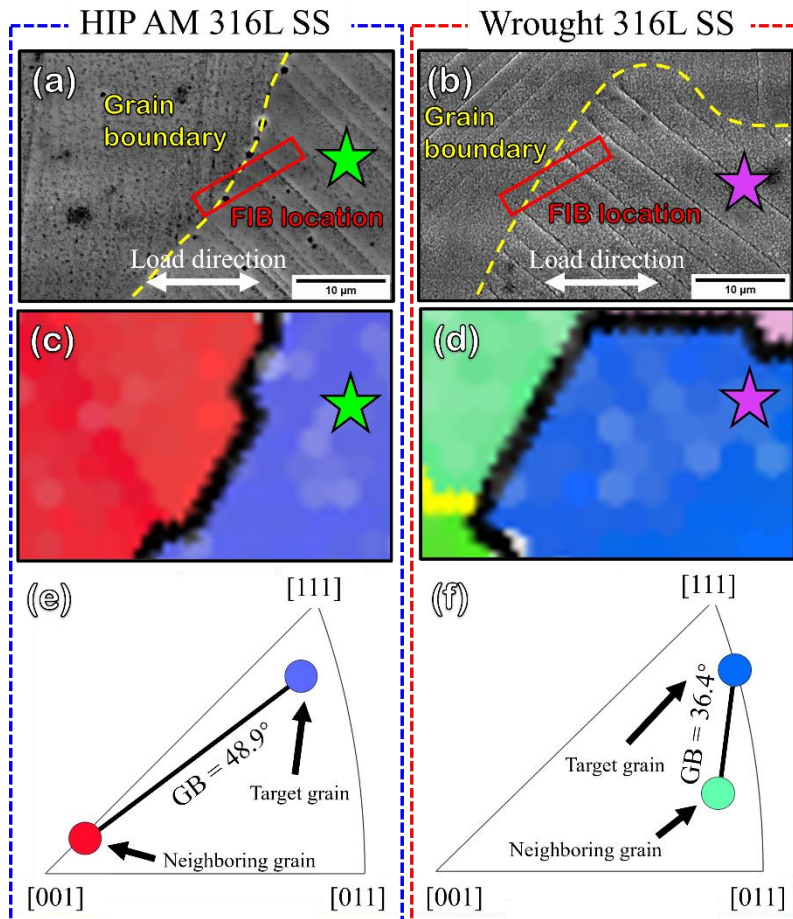


Fig. 7. Two comparable grains with dislocation channels terminated at the grain boundaries in HIP AM and wrought 316L SS. (a) and (b) are SEM images showing their GB-dislocation channel interactions; (c) and (d) are the corresponding EBSD IPF maps; (e) and (f) are the pole figures exhibiting the grain boundary angle and the grain orientation on both sides.

4.1.2. Dislocation channel broadening in HIP AM 316L SS

Fig. 8 shows the representative TEM bright field images of dislocation channels in HIP AM (Figs. 8(a) and (b)) and wrought (Figs. 8(c) and (d)) 316L SS after 6% of CERT. In Figs. 8(a) and (c), dislocation channels are identified as the dark straight bands. About 4-5 channels were involved in each TEM lamellae. The higher magnification images of an individual dislocation channel (Figs. 8(b) and (d)) revealed a channel comprised of multiple slip planes with ~10 nm spacing. We emphasize that the two materials showed a significant difference in channel width. As shown in Figs. 8(b) and (d), the channel width in HIP AM 316L SS is ~2-4 times wider than in wrought 316L SS. In the first set of TEM lamellae, HIP AM 316L SS showed an average channel width of 141.08 ± 73.41 nm, compared to 79.17 ± 23.93 nm in wrought 316L SS. In the other set, the average channel width in HIP AM and wrought 316L SS were 138.16 ± 47.92 nm and 38.48 ± 17.74 nm, respectively.

Although dislocation channeling has been extensively investigated for decades [27,28,59–61], limited studies considered the effect of channel broadening on stress localization near GBs and IASCC resistance. *Jiao et al.* [28] observed the expansion of dislocation channels near the dislocation channel-GB intersect and believed it would generate shear strain in GBs. A similar phenomenon was not found in the present study, but a shear step at the channel-GB intersect was observed from wrought 316L SS, suggesting a high local strain. In Fig. 9(b), the narrower channel in wrought 316L SS produced a shear perpendicular to the GB, which was not observed in HIP AM 316L SS (Fig. 9(a)). The shear deformation was responsible for a larger stress field in wrought 316L SS. If the shear step intersected with a GB at the surface, it could rupture the surface oxide film and promote crack initiation [24,62].

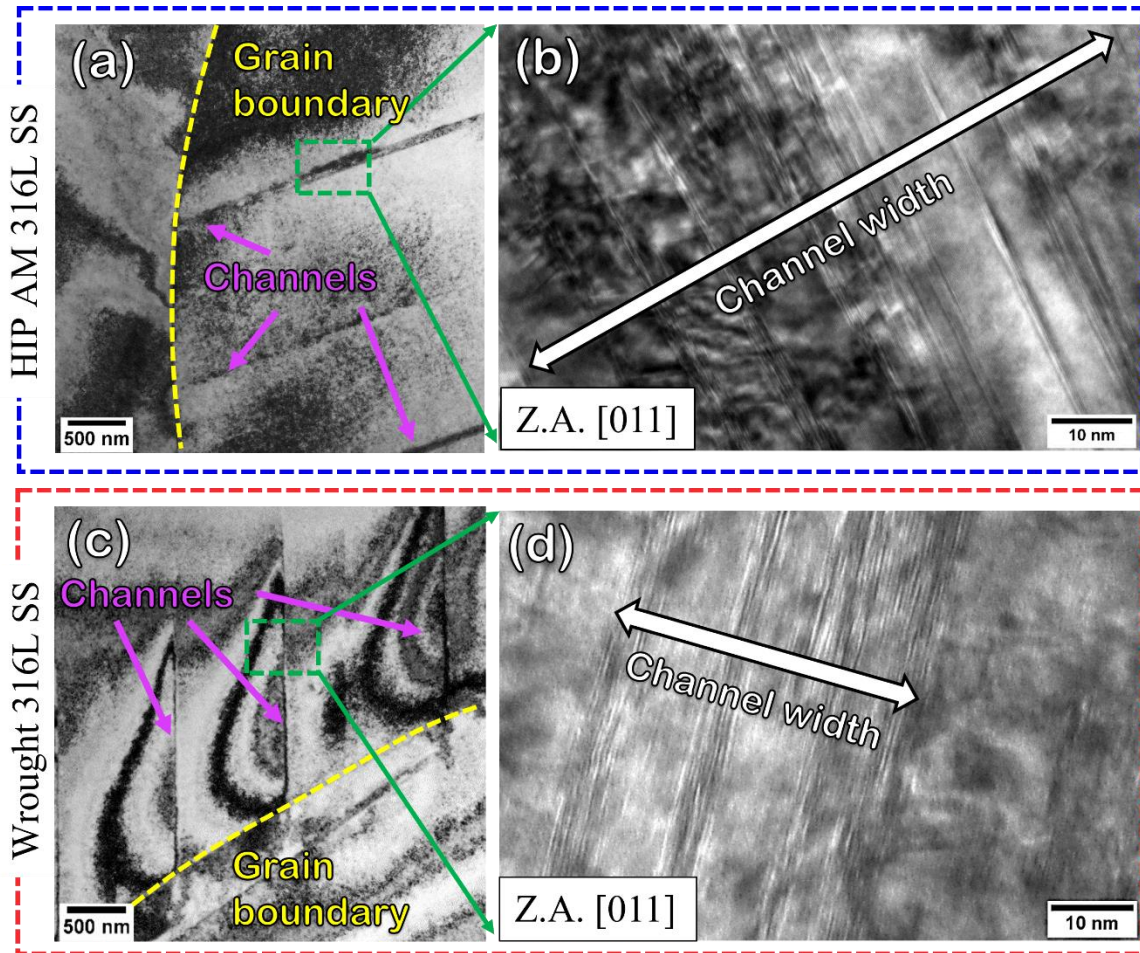


Fig. 8. TEM bright field images showing the morphology of dislocation channels in (a) and (b) HIP AM 316L SS, (c) and (d) wrought 316L SS after 6% of CERT test. The two locations were selected based on the grain selection criteria described in the section.

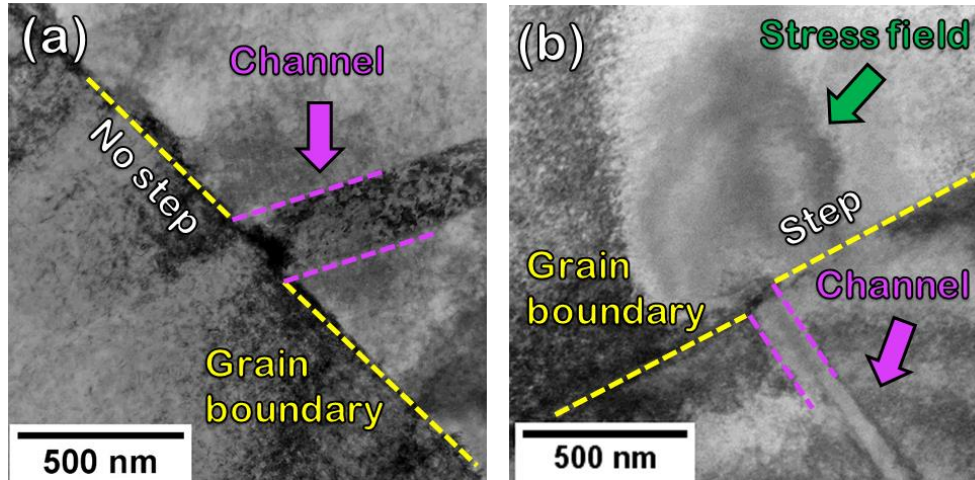


Fig. 9. STEM bright field images showing the dislocation channel-GB intersection in (a) HIP AM and (b) wrought 316L SS after 6% CERT test. The comparison suggests a high strain in the GB induced by the step due to dislocation channel-GB interaction in wrought 316L SS.

4.1.3. High-resolution TEM (HRTEM) characterization on dislocation channels

Fig. 10 shows the HRTEM view inside a dislocation channel in HIP AM 316L SS, taken from the same TEM lamella depicted above. Stacking faults (SFs) (Fig. 10(e)) and dislocations (Fig. 10(d)) were present in these slip bands. Deformation-produced martensite or twins were not found, and the selected area diffraction (SAD) (Fig. 10(a)) only revealed the austenitic phase. Dislocation channeling is believed to be the dominant deformation mechanism for HIP AM 316L SS. As a comparison, besides SFs and dislocations (Fig.10(d)), fine nanotwins with the thickness of a few atomic layers were observed in the dislocation channel of wrought 316L SS (Figs. 11(b) and (c)). The SAD in Fig. 11(a) further confirmed the formation of nanotwins. We note other studies also reported nanotwins formation from irradiated and deformed 316 and 316LN SS [35,63–65], suggesting a higher than normal strain localization within these channels.

We emphasize that the plastic flow is primarily localized within several slip bands along $\{111\}$ slip planes in wrought 316L SS (Fig. 11(a)), while the deformation is more uniform in the channels of HIP AM 316L SS (Fig. 10(a)). Although SFs were observed from HIP AM 316L SS, they were not highly concentrated in distinct bands. *Sharp* [61] observed a uniform glide of dislocations within the channels from irradiated high-purity copper, similar to the deformation of unirradiated materials. The channels were later confirmed to contain a low defect density, demonstrating that defects within channels played a role. Recent work [59] revealed that a certain level of dislocation

debris still existed in channels after straining. Thus, it is possible that the dislocations interacted with the remnant obstacles differently, resulting in different strain localization behavior even within a well-formed dislocation channel.

The formation of twins within the dislocation channel also requires a relatively high level of applied stress. *Byun* [66] summarized that the deformed microstructures based on the applied stress from low to high are dislocation tangles/pileups (200-400 MPa), isolated SFs/dislocations (400-600 MPa), and large stacking faults/twins/dislocations (600-900 MPa), indicating a higher localized stress within the channels in the wrought 316L SS. It is agreed that the formation of high-density nanotwins in FCC metals is contributed by the multiplication of Shockley partial dislocations with the same sign on successive $\{111\}$ planes [66–68]. The isolated spread of SFs in the HIP AM 316L SS suggests that the applied stress may not be high enough to facilitate SF multiplication, probably because of the channel broadening in the material (Fig. 8). SFE could be the intrinsic reason resulting in the difference, which will be discussed in the following section.

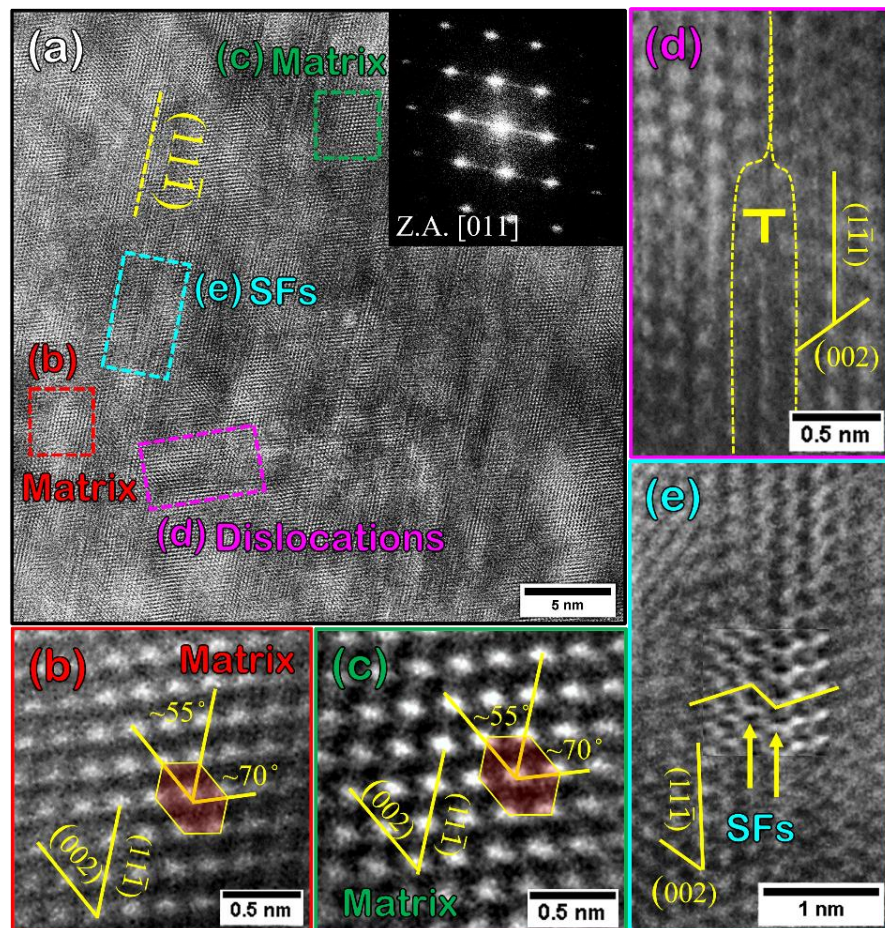


Fig. 10. (a) HRTEM image of a dislocation channel in irradiated HIP AM 316L SS after 6% CERT test in high-temperature water. (b) Matrix, (c) matrix from a different location, (d) dislocation, (e) stacking faults (SFs) with higher magnifications.

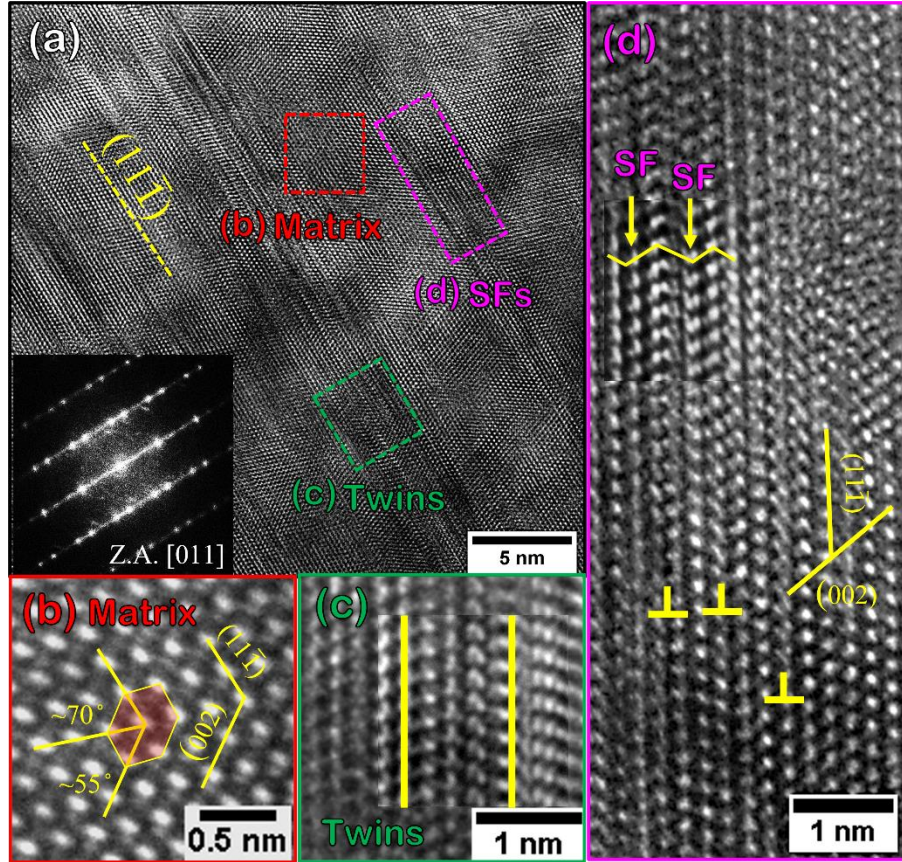


Fig. 11. (a) HRTEM image of a dislocation channel in irradiated wrought 316L SS after 6% CERT test in high-temperature water. (b) Matrix, (c) fine nanotwins, (d) stacking faults (SFs) and dislocations with higher magnifications.

4.2. Strain estimation in dislocation channels

The strain accumulation inside a dislocation channel was quantified by measuring the morphology of the dislocation channel from the sample surface using AFM. *Was et al.* [60] characterized the shear strain within a channel by calculating the channel height divided by the channel width. Supplementary Fig. S5 exhibits an example of measuring the channel height and width by AFM. It should be noted that the measured height (h') and width (w') need to be converted to the actual channel height (h) and width (w) by the following equations:

$$w = w' \sin(\delta) - h' \cos(\delta) \quad \text{Eq. 4}$$

$$h = h' / \cos(\alpha) \quad \text{Eq. 5}$$

where δ is the angle between the dislocation channel and the sample surface, and α is the angle between the dislocation slip direction and the normal direction of the sample surface, as is shown in Supplementary Fig. S5(d).

Fig. 12 shows the calculated shear strain from the dislocation channels near the GBs in HIP AM and wrought 316L SS after 6% of the CERT test. Two locations (L1 and L2) from each material were studied. The selection of the studied grains followed the criteria depicted in the earlier section. The shear strain of each channel was calculated from 3-4 measurements of its height and width. The scattered strain data was due to the channels with relatively higher strain than the others, which were confirmed to be their representative behaviors. The channel shear strain in wrought 316L SS was found to be ~4-5 times higher than in HIP AM 316L SS. The average shear strain in the dislocation channel of wrought 316L SS reached 8.10 with a peak value of 16.17, shown in Fig. 12(a). Considering only 6% of the global tensile strain applied, the values suggest an extremely high strain localization near GBs. We note that it is common for the strain of a dislocation channel to reach >100 times that of the global strain [27,69]. *McMurtrey et al.* [20] reported ~500% strain from a dislocation channel of irradiated stainless steel with 4% plastic strain using a digital image correlation (DIC) method. The high strain localization in the wrought 316L SS is believed to promote crack initiation at GBs and is correlated well with the TEM observations.

With a similar global strain and channel spacing (Fig. 6) of HIP AM and wrought 316L SS, it implies that the plastic strain created by each individual channel in the two materials is comparable. However, due to the broadening of the channels in HIP AM 316L SS, the local plastic strain of a channel was spread across the wider range, resulting in a broader channel width and less channel height. The local microstructure can be explained by Fig. 8. The broader channel in HIP AM material is comprised of a larger number of nanoscale slips. In contrast, the deformation in the wrought material exhibited narrower channels with more concentrated slips, resulting in larger local channel height.

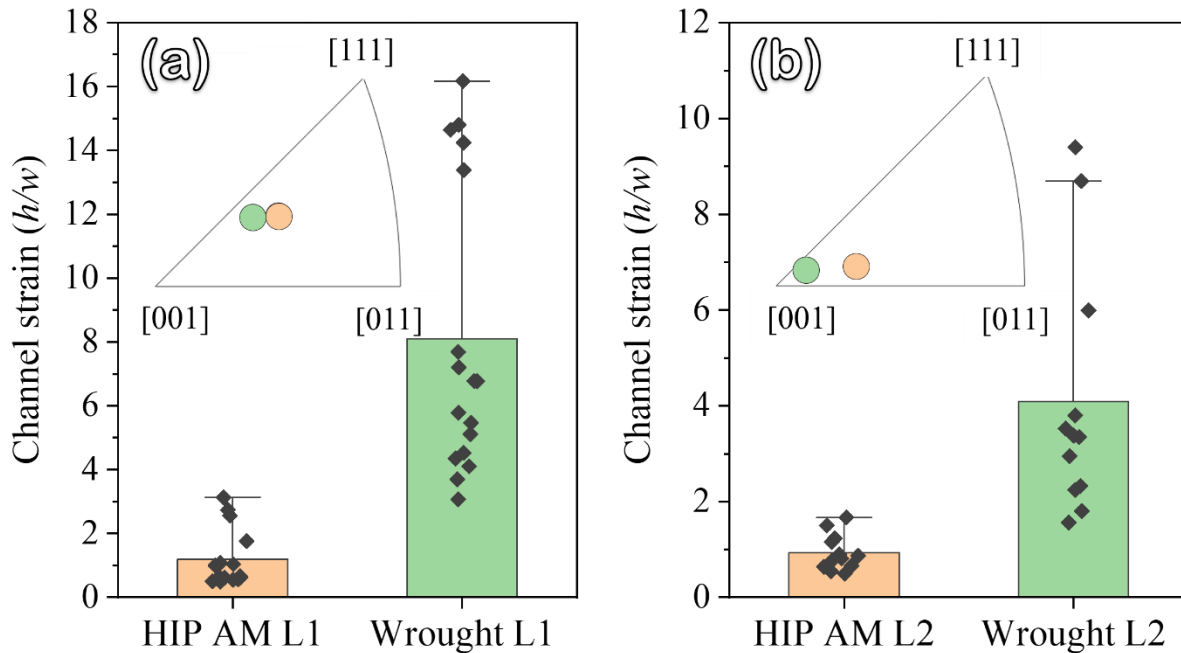


Fig. 12. The strain of dislocation channels in HIP AM and wrought 316L SS after 6% of CERT test. (a) and (b) show the results from two groups of comparable grains following the grain selection criteria (L1: comparable location 1; L2: comparable location 2). The pole figure presented the grain orientations for each group. The results suggest that the strain within the dislocation channels in wrought 316L SS is ~4-5 times higher than in the HIP AM 316L SS.

4.3. Further understanding of dislocation channel broadening

4.3.1. The effect of defect distribution on channel broadening by stochastic simulation

Radiation induced defects as the intrinsic factor of constrained plastic flow in irradiated alloys were also found to affect dislocation channel width through multiple mechanisms, such as the double cross-slip caused by the interaction with SFTs [70,71] or the point defect annihilation [72]. Doyle *et al.* [33] developed a model to predict the channel width as a function of defect size, density, and distance from the source. The model assumed the defect cluster could be completely absorbed, resulting in the dislocation jog to a distance equal to half of the size of defect clusters. Therefore, the defect size controls the jog distance, while the density governs the interaction frequency.

Fig. 13 shows the simulated channel width by the aforementioned model as a function of defect size and density. The plot illustrates that the increase in defect size and density would lead to channel broadening. However, it should be noted that the channel width is less sensitive to defect

size towards lower defect density, especially less than $5 \times 10^{21}/\text{m}^3$. As marked in Fig. 13, the dislocation channels formed with a lower defect density but a larger defect size can be narrower than those formed with a high defect density and a finer defect size. This phenomenon correlates well with the experimental observations in HIP AM and wrought 316L SS in this study. HIP AM 316L SS presented smaller-sized but higher-density dislocation loops, resulting in wider channels than wrought 316L SS (Table 2). The simulation suggests that even though the defect size is small, a higher density of defects may still significantly enhance dislocation cross-slip frequency, resulting in broader channels.

We note that the simulation may still present an inaccurate prediction of a real material system in this study due to many factors, including neglecting the developed defects such as nanotwins and SFs, the effects from the crystal structure and cross-slip energy, simplifying the assumptions of jump frequency and dislocation-defect interaction, *etc.* [33]. SFE is believed to significantly affect the deformation mode by controlling dislocation cross-slip. For the materials with low SFE, dislocation channeling was found to be accompanied by deformation twinning as an alternative deformation mechanism [35]. The formation of twins could further retard dislocation glide and induce work hardening within dislocation channels, resulting in the constrained development of the channel width [35]. *Doyle et al.* [33] also mentioned that the model may be insufficient to predict the channel width with multiple deformation mechanisms working simultaneously, which could be the case in the present study. In fact, a similar overestimation in channel width was reported by feeding *Farrell's et al.*[35,36] stainless steel data in the model [33].

Source widening and dislocation multiplication were not considered in the model since the simulation only emitted dislocations from a fixed location one at a time. The HIP AM 316L SS contained more oxide inclusions (Fig. 2), which could potentially serve as the dislocation source that contributed to the channel broadening. While *Doyle et al.* [33] simulated the source widening by increasing the number of dislocation sources and believed the effect was minor, detailed studies with more realistic dislocation source size and distance are still necessary to confirm it. Dislocation multiplication could also play a role in channel width, especially for the multiplication at the edge of the channels. People believe that the tangled dislocations at the channel edge could initiate Frank-Read sources, which would further expand the channel width [59]. More advanced tools or models are needed to simulate these effects on dislocation channel broadening.

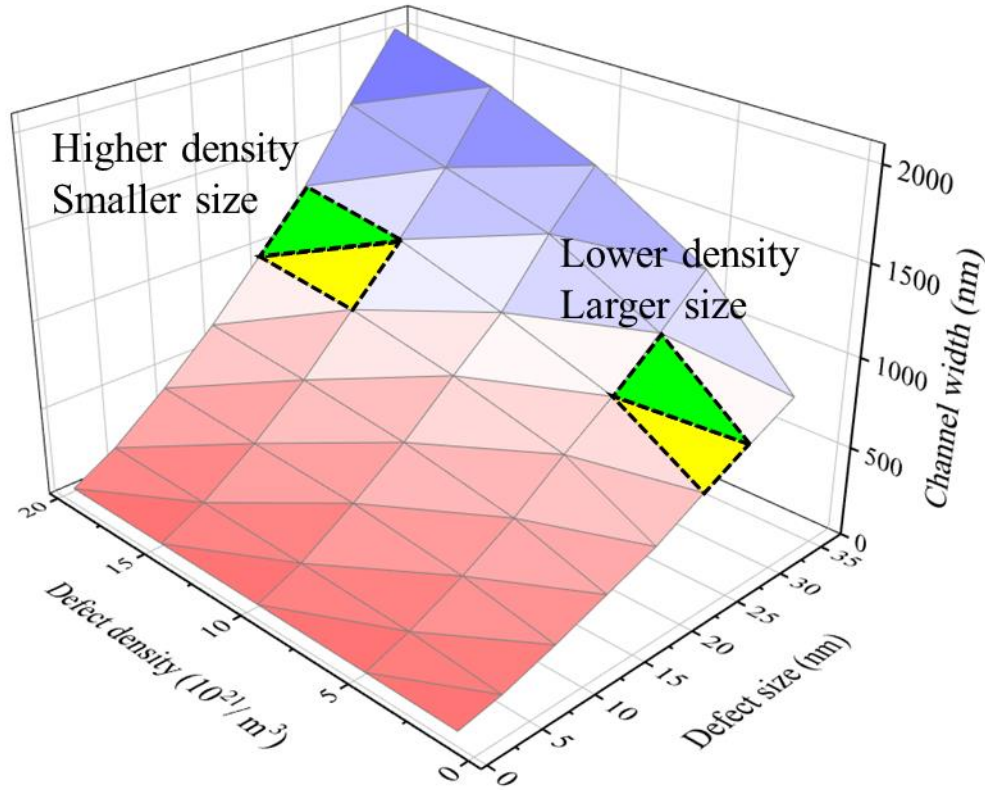


Fig. 13. Effect of irradiation induced defect size and density on channel width produced by simulation. Two pairs of zones are highlighted, representing that channels formed with a higher defect density but a smaller size could be broader than those formed with a lower density but a larger size.

4.3.2. The effect of radiation induced precipitates/clusters on channel broadening

Previous work [11] reported radiation induced γ' precipitates from both HIP AM and wrought 316L SS. The γ' precipitates in HIP AM and wrought 316L SS are similar in terms of the size (6.6 ± 1 nm vs. 7.8 ± 1 nm) and the density ($2.9 \pm 0.3 \times 10^{21}/\text{m}^3$ vs. $2.2 \pm 0.2 \times 10^{21}/\text{m}^3$). The formation of γ' precipitates is believed to stem from RIS at defect sites, such as line dislocations, dislocation loops, and oxide-matrix interface [11,73,74]. Besides γ' precipitates, STEM-EDX also revealed a high density of Ni-Si clusters around the γ' particles in irradiated HIP AM 316L SS. Such phenomenon was not observed in wrought material, as is shown in Fig. 14. It is rather challenging to quantify the size and density of the Ni-Si clusters due to their irregular morphologies. The formation of the Ni-Si cluster is believed as a result of RIS at radiation induced defects or vacancies [74,75]. It is known that Ni-Si clustering generally starts around imperfections, like dislocation loops or grain boundaries. HIP AM 316L SS has much higher loop density, thus clustering is

widely spread across the material. When local concentration is beyond the solute solubility, precipitation can occur, producing larger precipitates. We believe a wider spread of Ni-Si clustering in HIP AM 316L SS, caused by high-density dislocation loops, delayed local supersaturation which further affected precipitation. In addition, we note HIP AM 316L SS contains a higher level of Si than wrought 316L SS as shown in Table 1, which may be linked to the Ni-Si clustering.

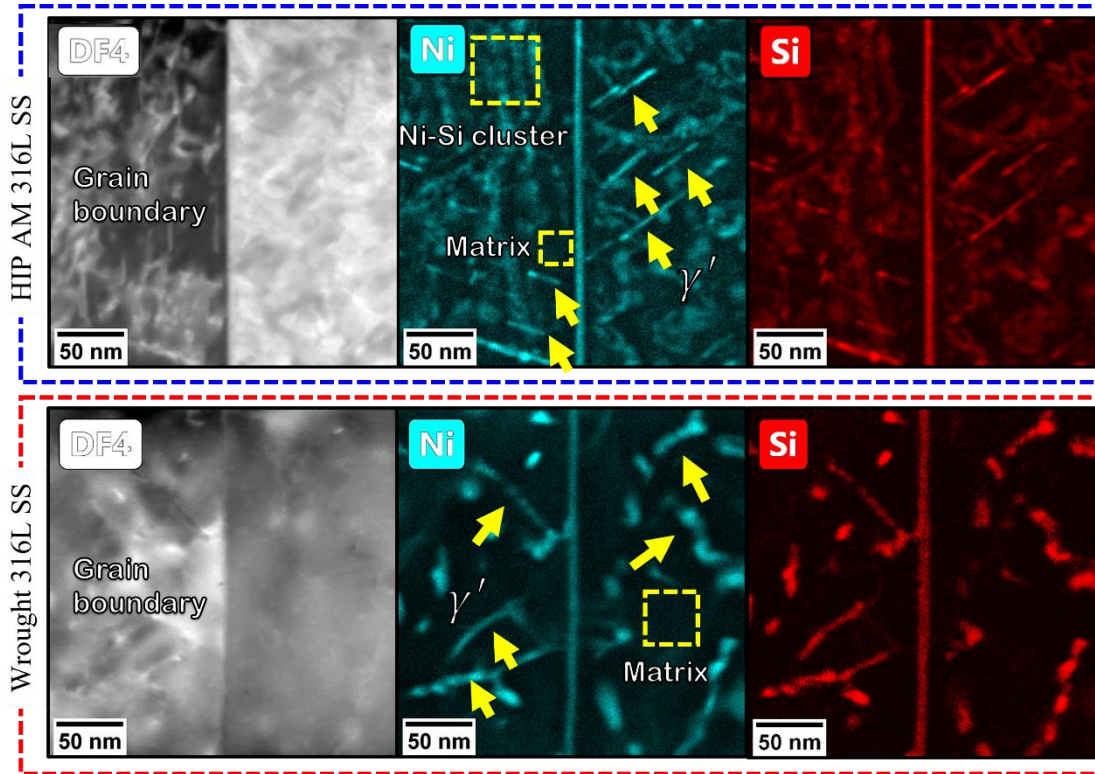


Fig. 14. STEM dark field (DF) image and the associated Ni and Si EDX mappings of proton irradiated HIP AM and wrought 316L SS. A high density of Ni-Si cluster was observed around the γ' precipitates in HIP AM 316L SS, while the mappings of wrought 316L SS mostly revealed γ' precipitates.

Compared with dislocation loops, γ' precipitates and Ni-Si clusters are weak barriers to dislocation motion [51]. Hence, their direct effect on deformation is minor. However, it is possible that a high density of Ni-Si clusters could alter the local SFE. It is well known that SFE is associated with dislocation cross-slip behaviors. Extensive studies revealed that high SFE caused less slip planarity or even changed the deformation mode from planar slip to wavy slip in irradiated materials, reducing the strain/stress localization and enhancing the IASCC resistance [24,30,74,76].

The chemical compositions of the Ni-Si clusters, the steel matrix of HIP AM 316L SS, and the steel matrix of wrought 316L SS were measured by STEM-EDX, as listed in Table 4. The SFEs were estimated based on Eq. 6 [77] shown as follows:

$$\gamma = -7.1 + 2.8Ni + 0.49Cr + 2.0Mo - 2.0Si + 0.75Mn \quad \text{Eq. 6}$$

In Table 4, the SFEs suggest an increase in SFEs due to the formation of the Ni-Si clusters. *Whelan et al.* [78,79] measured the SFE of 15-30 mJ/m² from the stainless steels with the Cr content of 18-20 wt.% and Ni content of 8-11 wt.%, similar to the matrix composition of HIP AM and wrought 316L SS. *Yonezawa et al.* [77] reported an SFE of 43.4 mJ/m² from a solution annealed 13.35Cr-15.51Ni-1.82Si SS followed by water quench, which is close to the composition of the Ni-Si clusters. Therefore, it is reasonable to believe that the SFE of the Ni-Si clusters is 10-15 mJ/m² higher than the matrix.

Previous studies suggested the predominance of dislocation slip happened with the SFE higher than 50 mJ/m² in stainless steels, while a mixture of twinning and slip is more common with the SFE from 15-50 mJ/m² [74]. It was also reported [28,66] that the stress required for twinning is directly proportional to SFE. That is, deformation twins are hard to form in the alloy with a high SFE. As a result, considering the different deformation behavior of HIP AM vs. wrought 316L SS (Fig. 10 and Fig. 11), it is possible that the wide distribution of Ni-Si clusters in HIP AM 316L SS facilitate the dislocation cross-slip and decreased slip planarity, resulting in the channel broadening.

Table 4. Chemical compositions of HIP AM 316L SS matrix, HIP AM 316L SS Ni-Si cluster, and wrought 316L SS matrix measured by STEM-EDX.

Element (wt.%)	Fe	Cr	Ni	Si	Mn	Mo	SFE (mJ/m ²)
HIP AM 316L SS matrix	Bal.	18.67 ±0.34	9.02 ±0.34	0.71 ±0.05	2.07 ±0.01	5.88 ±0.52	37.30 ± 0.22
HIP AM 316L SS Ni-Si cluster	Bal.	14.86 ±0.68	14.42 ±1.02	1.78 ±0.31	1.60 ±0.01	3.55 ±0.35	45.29 ± 1.67
Wrought 316L SS matrix	Bal.	19.00 ±0.12	8.71 ±0.50	0.76 ±0.10	1.99 ±0.06	5.36 ±0.52	42.62 ± 2.13

4.4. Possible reasons for the defect formation differences in HIP AM vs. wrought 316L SS

It remains unclear why radiation-induced defects formed differently in HIP AM 316L SS as compared to the wrought counterpart. This question is mainly centered on dislocation loops, as Ni-Si clustering/precipitation is associated to different loop distributions. While the mechanistic causes of different defect distributions of HIP AM vs. wrought 316L SS is not the focus of this work, we believe two factors may contribute to the differences. First, the minor chemical composition difference, such as Si, could result in different damage responses. HIP AM 316L SS contained 0.71 wt.% of Si, as compared with 0.35 wt.% of Si in the wrought material. The higher Si content in HIP AM 316L SS could promote nucleation of dislocation loops, resulting in higher loop density and RIS on the defects. Studies [80–82] revealed that a minor amount of Si addition (0.3 wt.% or less) in stainless steel could promote interstitial loop nucleation, as it was found to bind with interstitials and increase the activation energy for loop formation. However, some other studies [28,83] reported suppression of radiation damage in stainless steel due to Si addition. They believed Si enhanced vacancy diffusivity as an undersized solute and promoted interstitial-vacancy recombination. In fact, our characterizations of void swelling are consistent with this perspective, as they were found to be suppressed in HIP AM 316L SS (Table 2). The consensus on the Si effect on radiation damage is yet to be reached.

We note that some work has been done to study the effects of minor elements (including Si) on IASCC in wrought 316L SS, which did not show similar IASCC mitigation [48,50,53]. The conclusions from these work were mixed. Therefore, we believe the difference may also be attributed to the characteristics of HIP AM 316L SS. Even after HIP, residual dislocations (Figs. S6(a) and (b)), local minor chemical segregation (Cr, Mo, S) on GBs, and oxides were still present in HIP AM 316L SS. It was surprising to us that these features remained in HIP AM 316L SS even after multiple high-temperature treatments. Inside the grains, dislocations were patterned in lines with intercept angles near 60° , clearly representing the difficult cross-slip between slip planes. We note this phenomenon may also be observed in fully-annealed wrought counterpart, but generally with less density. Near the GBs, dislocations were clustered in HIP AM 316L SS as well. It is known that pre-existing defects and chemical disorders (residual dislocation, chemical segregation, and oxides) can alter radiation defect nucleation and growth. One example is that the oxides in HIP or fully annealed AM SSs could suppress void swelling [11,84].

The contributions from minor alloy elements, low-level residual dislocations, local chemical segregation, and oxides to radiation damage (mainly loop nucleation in this study) are complex and have not yet been clearly understood for wrought material systems. The present study primarily focused on dislocation channel broadening as an alternative mechanism of IASCC. More work is needed to identify if the different radiation damage responses stem purely from the chemical compositions, or if the dislocation defects or chemical segregations in AM materials also play a role. It would be necessary to look at different heats of AM 316L SS and wrought 316L SS to support the ongoing development of nuclear AM specification to guide how AM 316L SS should be formulated, fabricated, and post-AM processed.

4.5. A summary of physical insights

Fig. 15 depicts the different types of dislocation channel-GB interactions in (a) unirradiated 316L SS, (b) irradiated wrought 316L SS, and (c) irradiated HIP AM 316L SS, respectively. It is known that deformation is uniform in unirradiated material when radiation-induced defects or obstacles are not present. In the irradiated wrought and HIP AM 316L SS, plastic flow was constrained to form dislocation channels. Channel broadening in HIP AM 316L SS resulted in less strain localization inside channels and on GBs. We believe that the way defects were distributed in terms of their density and size in HIP AM 316L SS caused more frequent dislocation cross-slip, leading to broader channels. To compound this effect, Ni-Si clusters in HIP AM 316L SS increased the local SFE and the stress required for twinning, facilitating the dislocation cross-slip, and suppressing twinning. During deformation, the stress is highly confined in the channels in wrought 316L SS, promoting twin formation.

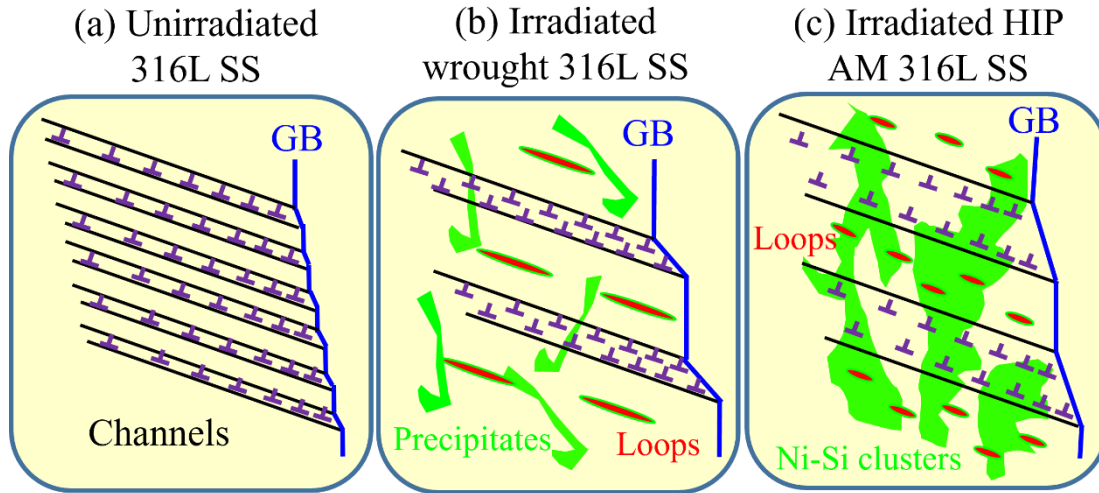


Fig. 15. Schematics of dislocation channel-GB interactions in (a) unirradiated 316L SS; (b) irradiated wrought 316L SS; (c) irradiated HIP AM 316L SS. The dislocation loops are highlighted red, and the Ni-Si rich precipitates and clusters are colored green.

5. Conclusions and Perspectives

For the first time, this study highlights the importance of dislocation channel broadening on IASCC susceptibility of 316L SS and provides direct experimental evidence based on commercial-grade materials. Channel broadening serves as the main mechanism for the superior IASCC resistance of HIP AM 316L SS as compared to wrought 316L SS in high-temperature water, originating from the reduced strain localization inside the channels and on the GBs. The distribution of radiation induced defects in terms of their density and size in HIP AM 316L SS makes dislocation cross-slip more frequent, thus producing broader channels. To compound this effect, the formation of Ni-Si clusters in HIP AM 316L SS increased the local SFE, facilitating dislocation cross-slip and suppressing twin formation during deformation, both of which assist channel broadening.

This study also confirms that radiation hardening may not be a reliable measure for IASCC susceptibility of 316L SS. The nuclear industry is evaluating radiation hardening as a tool to evaluate IASCC susceptibility. However, a contradictory trend is shown in Fig. 5, where 316L SS with more significant radiation hardening yields lower IASCC susceptibility. Strain localization on GBs through dislocation channeling is the key driving mechanism for IASCC initiation.

Although this new mechanism of improving IASCC resistance was obtained from 316L SS made by LPBF AM, we believe it is applicable to 316L SS in other forms, and even different engineering alloy systems. At the same radiation dose, this mechanism promises the opportunity to reduce IASCC susceptibility of an engineering alloy by broadening the dislocation channels through altering defect distribution. Further studies are required to understand the relationship between steel chemistry, defect distribution, channel broadening, and processing conditions.

Acknowledgements

This research is mainly supported by Nuclear Science User Facilities (NSUF) Rapid Turnaround Experiments (RTE) and the Idaho National Laboratory's Laboratory Directed Research and Development (LDRD) program under DOE Idaho Operations Office Contract DE-AC07-05ID14517, and the Nuclear Energy University Program (NEUP) of the Office of Nuclear Energy, the U.S. Department of Energy under the contract DE-NE0009193. The work is also supported by the U.S. Nuclear Regulatory Commission (NRC) under the research grant NRC-31310021M0047. Authors thank the Michigan Ion Beam Laboratory at the University of Michigan for proton irradiation experiment and Dr. Gary Was for the helpful discussion.

References

- [1] H. Yin, M. Song, P. Deng, L. Li, B.C. Prorok, X. Lou, Thermal stability and microstructural evolution of additively manufactured 316L stainless steel by laser powder bed fusion at 500-800 °C, *Addit. Manuf.* (2021).
- [2] P. Deng, M. Song, J. Yang, Q. Pan, S. McAllister, L. Li, B.C. Prorok, X. Lou, On the thermal coarsening and transformation of nanoscale oxide inclusions in 316L stainless steel manufactured by laser powder bed fusion and its influence on impact toughness, *Mater. Sci. Eng. A.* 835 (2022) 142690. <https://doi.org/10.1016/j.msea.2022.142690>.
- [3] X. Lou, P.L. Andresen, R.B. Rebak, Oxide inclusions in laser additive manufactured stainless steel and their effects on impact toughness and stress corrosion cracking behavior, *J. Nucl. Mater.* 499 (2018) 182–190. <https://doi.org/10.1016/j.jnucmat.2017.11.036>.
- [4] B. Barkia, P. Aubry, P. Haggi-Ashtiani, T. Auger, L. Gosmain, F. Schuster, H. Maskrot, On the origin of the high tensile strength and ductility of additively manufactured 316L stainless steel: Multiscale investigation, *J. Mater. Sci. Technol.* 41 (2020) 209–218. <https://doi.org/10.1016/j.jmst.2019.09.017>.
- [5] S. Dryepondt, P. Nandwana, P. Fernandez-Zelaia, F. List, Microstructure and high

- temperature tensile properties of 316L fabricated by laser powder-bed fusion, *Addit. Manuf.* 37 (2021) 101723. <https://doi.org/10.1016/j.addma.2020.101723>.
- [6] M. Song, C.R. Lear, C.M. Parish, M. Wang, G.S. Was, Radiation tolerance of commercial and advanced alloys for core internals: a comprehensive microstructural characterization, *J. Nucl. Mater.* 510 (2018) 396–413. <https://doi.org/10.1016/j.jnucmat.2018.08.035>.
- [7] M. Song, J. Yang, X. Liu, L.R. Hawkins, Z. Jiao, L. He, Y. Zhang, D. Schwen, X. Lou, Void swelling in additively manufactured 316L stainless steel with Hafnium composition gradients under self-ion irradiation, *J. Nucl. Mater.* (2023) 154351. <https://doi.org/10.1016/j.jnucmat.2023.154351>.
- [8] J. Yang, X. Liu, M. Song, L. He, S. Bankson, M. Hamilton, B. Prorok, X. Lou, Sensitization, desensitization, and carbide evolution of Alloy 800H made by laser powder bed fusion, *Addit. Manuf.* 50 (2021) 102547. <https://doi.org/10.1016/j.addma.2021.102547>.
- [9] J. Yang, M. Song, L.R. Hawkins, X. Liu, L. He, X. Lou, Effects of heat treatment on corrosion fatigue and stress corrosion crack growth of additive-manufactured Alloy 800H in high-temperature water, *Corros. Sci.* 191 (2021) 109739. <https://doi.org/10.1016/j.corsci.2021.109739>.
- [10] X. Lou, M. Song, P.W. Emigh, M.A. Othon, P.L. Andresen, On the stress corrosion crack growth behaviour in high temperature water of 316L stainless steel made by laser powder bed fusion additive manufacturing, *Corros. Sci.* 128 (2017) 140–153. <https://doi.org/10.1016/j.corsci.2017.09.017>.
- [11] M. Song, M. Wang, X. Lou, R.B. Rebak, G.S. Was, Radiation damage and irradiation-assisted stress corrosion cracking of additively manufactured 316L stainless steels, *J. Nucl. Mater.* 513 (2019) 33–44. <https://doi.org/10.1016/j.jnucmat.2018.10.044>.
- [12] J. Yang, L. Hawkins, L. He, S. Mahmood, M. Song, K. Schulze, X. Lou, Intragranular irradiation-assisted stress corrosion cracking (IASCC) of 316L stainless steel made by laser direct energy deposition additive manufacturing : Delta ferrite-dislocation channel interaction, *J. Nucl. Mater.* 577 (2023) 154305. <https://doi.org/10.1016/j.jnucmat.2023.154305>.
- [13] M. McMurtrey, C. Sun, R.E. Rupp, C.H. Shiau, R. Hanbury, N. Jerred, R. O'Brien, Investigation of the irradiation effects in additively manufactured 316L steel resulting in decreased irradiation assisted stress corrosion cracking susceptibility, *J. Nucl. Mater.* 545 (2021). <https://doi.org/10.1016/j.jnucmat.2020.152739>.
- [14] M. Hiser, A. Schneider, M. Audrain, A. Hull, Regulatory Research Perspective on Additive Manufacturing for Nuclear Component Applications, *J. Nucl. Mater.* 546 (2021) 152726. <https://doi.org/10.1016/j.jnucmat.2020.152726>.
- [15] C.H. Shiau, M.D. McMurtrey, R.C. O'Brien, N.D. Jerred, R.D. Scott, J. Lu, X. Zhang, Y. Wang, L. Shao, C. Sun, Deformation behavior and irradiation tolerance of 316 L stainless steel fabricated by direct energy deposition, *Mater. Des.* 204 (2021) 109644. <https://doi.org/10.1016/j.matdes.2021.109644>.

- [16] S.M. Bruemmer, G.S. Was, Microstructural and microchemical mechanisms controlling intergranular stress corrosion cracking in light-water-reactor systems, *J. Nucl. Mater.* 216 (1994) 348–363. [https://doi.org/10.1016/0022-3115\(94\)90020-5](https://doi.org/10.1016/0022-3115(94)90020-5).
- [17] S.M. Bruemmer, E.P. Simonen, Radiation Hardening and Radiation-Induced Chromium Depletion Effects on Intergranular Stress Corrosion Cracking in Austenitic Stainless Steels, *Corros. Sci.* (1994) 940–946.
- [18] S.M. Bruemmer, E.P. Simonen, P.M. Scott, P.L. Andresen, G.S. Was, J.L. Nelson, Radiation-induced material changes and susceptibility to intergranular failure of light-water-reactor core internals, *J. Nucl. Mater.* 274 (1999) 299–314. [https://doi.org/10.1016/S0022-3115\(99\)00075-6](https://doi.org/10.1016/S0022-3115(99)00075-6).
- [19] G.S. Was, J.T. Busby, Role of irradiated microstructure and microchemistry in irradiation-assisted stress corrosion cracking, *Philos. Mag.* 85 (2005) 443–465. <https://doi.org/10.1080/02678370412331320224>.
- [20] M.D. McMurtrey, G.S. Was, B. Cui, I. Robertson, L. Smith, D. Farkas, Strain localization at dislocation channel–grain boundary intersections in irradiated stainless steel, *Int. J. Plast.* 56 (2014) 219–231. <https://doi.org/10.1016/j.ijplas.2014.01.001>.
- [21] M.D. McMurtrey, G.S. Was, L. Patrick, D. Farkas, Relationship between localized strain and irradiation assisted stress corrosion cracking in an austenitic alloy, *Mater. Sci. Eng. A.* 528 (2011) 3730–3740. <https://doi.org/10.1016/j.msea.2011.01.073>.
- [22] Z. Jiao, G.S. Was, Impact of localized deformation on IASCC in austenitic stainless steels, *J. Nucl. Mater.* 408 (2011) 246–256. <https://doi.org/10.1016/j.jnucmat.2010.10.087>.
- [23] J. Yang, L. Hawkins, M. Song, L. He, M. Bachhav, Q. Pan, L. Shao, D. Schwen, X. Lou, Compositionally graded specimen made by laser additive manufacturing as a high-throughput method to study radiation damages and irradiation-assisted stress corrosion cracking, *J. Nucl. Mater.* 560 (2021) 153493. <https://doi.org/10.1016/j.jnucmat.2021.153493>.
- [24] G.S. Was, B. Alexandreanu, J. Busby, Localized deformation induced IGSCC and IASCC of austenitic alloys in high temperature water, *Key Eng. Mater.* 261–263 (2004) 885–902. <https://doi.org/10.4028/www.scientific.net/kem.261-263.885>.
- [25] Y. Matsukawa, Y.N. Osetsky, R.E. Stoller, S.J. Zinkle, Mechanisms of stacking fault tetrahedra destruction by gliding dislocations in quenched gold, *Philos. Mag.* 88 (2008) 581–597. <https://doi.org/10.1080/14786430801898644>.
- [26] C.R.F. Azevedo, A review on neutron-irradiation-induced hardening of metallic components, *Eng. Fail. Anal.* 18 (2011) 1921–1942. <https://doi.org/10.1016/j.engfailanal.2011.06.008>.
- [27] T. Byun, N. Hashimoto, Strain Localization in Irradiated Materials, *Nucl. Eng. Technol.* 38 (2006) 619–638.
- [28] Z. Jiao, J.T. Busby, G.S. Was, Deformation microstructure of proton-irradiated stainless steels, *J. Nucl. Mater.* 361 (2007) 218–227. <https://doi.org/10.1016/j.jnucmat.2006.12.012>.

- [29] Z. Jiao, M.D. McMurtrey, G.S. Was, Strain-induced precipitate dissolution in an irradiated austenitic alloy, *Scr. Mater.* 65 (2011) 159–162. <https://doi.org/10.1016/j.scriptamat.2011.04.003>.
- [30] Z. Jiao, G.S. Was, The role of irradiated microstructure in the localized deformation of austenitic stainless steels, *J. Nucl. Mater.* 407 (2010) 34–43. <https://doi.org/10.1016/j.jnucmat.2010.07.006>.
- [31] B. Cui, J. Kacher, M. McMurtrey, G. Was, I.M. Robertson, Influence of irradiation damage on slip transfer across grain boundaries, *Acta Mater.* 65 (2014) 150–160. <https://doi.org/10.1016/j.actamat.2013.11.033>.
- [32] M.D. McMurtrey, B. Cui, I. Robertson, D. Farkas, G.S. Was, Mechanism of dislocation channel-induced irradiation assisted stress corrosion crack initiation in austenitic stainless steel, *Curr. Opin. Solid State Mater. Sci.* 19 (2015) 305–314. <https://doi.org/10.1016/j.cossms.2015.04.001>.
- [33] P.J. Doyle, K.M. Benensky, S.J. Zinkle, Modeling of dislocation channel width evolution in irradiated metals, *J. Nucl. Mater.* 499 (2018) 47–64. <https://doi.org/10.1016/j.jnucmat.2017.10.063>.
- [34] T.S. Byun, N. Hashimoto, K. Farrell, E.H. Lee, Characteristics of microscopic strain localization in irradiated 316 stainless steels and pure vanadium, *J. Nucl. Mater.* 349 (2006) 251–264. <https://doi.org/10.1016/j.jnucmat.2005.10.011>.
- [35] K. Farrell, T.S. Byun, N. Hashimoto, Deformation mode maps for tensile deformation of neutron-irradiated structural alloys, *J. Nucl. Mater.* 335 (2004) 471–486. <https://doi.org/10.1016/j.jnucmat.2004.08.006>.
- [36] K. Farrell, T.S. Byun, N. Hashimoto, MAPPING FLOW LOCALIZATION PROCESSES IN DEFORMATION OF IRRADIATED REACTOR STRUCTURAL ALLOYS - FINAL REPORT, 2003. <http://www.osti.gov/servlets/purl/885795-jy25MJ/>.
- [37] R.B. Rebak, X. Lou, P.W. Emigh, M.A. Othon, P.L. Andresen, M. Song, M. Wang, Environmental Cracking and Irradiation Resistant Stainless Steels by Additive Manufacturing, *Bonisteel Blvd.* (2018) 1–98.
- [38] J.F. Ziegler, J.P. Biersack, SRIM 2013 Program, (n.d.).
- [39] P.L. Andresen, A brief history of environmental cracking in hot water, *Corrosion.* 75 (2019) 240–253. <https://doi.org/10.5006/2881>.
- [40] P.L. Andresen, G.S. Was, A historical perspective on understanding IASCC, *J. Nucl. Mater.* 517 (2019) 380–392. <https://doi.org/10.1016/j.jnucmat.2019.01.057>.
- [41] P. Dong, F. Vecchiato, Z. Yang, P.A. Hooper, M.R. Wenman, The effect of build direction and heat treatment on atmospheric stress corrosion cracking of laser powder bed fusion 316L austenitic stainless steel, *Addit. Manuf.* 40 (2021) 101902. <https://doi.org/10.1016/j.addma.2021.101902>.
- [42] K. Chadha, Y. Tian, J.G. Spray, C. Aranas, Effect of annealing heat treatment on the microstructural evolution and mechanical properties of hot isostatic pressed 316L stainless

- steel fabricated by laser powder bed fusion, *Metals (Basel)*. 10 (2020) 1–18.
<https://doi.org/10.3390/met10060753>.
- [43] G. Álvarez, Z. Harris, K. Wada, C. Rodríguez, E. Martínez-Pañeda, Hydrogen embrittlement susceptibility of additively manufactured 316L stainless steel: Influence of post-processing, printing direction, temperature and pre-straining, *Addit. Manuf.* 78 (2023) 103834. <https://doi.org/10.1016/j.addma.2023.103834>.
- [44] P. Deng, M. Karadge, R.B. Rebak, V.K. Gupta, B.C. Prorok, X. Lou, The origin and formation of oxygen inclusions in austenitic stainless steels manufactured by laser powder bed fusion, *Addit. Manuf.* 35 (2020) 101334.
<https://doi.org/10.1016/j.addma.2020.101334>.
- [45] M. Wang, M. Song, C.R. Lear, G.S. Was, Irradiation assisted stress corrosion cracking of commercial and advanced alloys for light water reactor core internals, *J. Nucl. Mater.* 515 (2019) 52–70. <https://doi.org/10.1016/j.jnucmat.2018.12.015>.
- [46] T. Kato, H. Takahashi, M. Izumiya, Grain boundary segregation under electron irradiation in austenitic stainless steels modified with oversized elements, *J. Nucl. Mater.* 189 (1992) 167–174. [https://doi.org/10.1016/0022-3115\(92\)90529-T](https://doi.org/10.1016/0022-3115(92)90529-T).
- [47] L. Fournier, B.H. Sencer, G.S. Was, E.P. Simonen, S.M. Bruemmer, The influence of oversized solute additions on radiation-induced changes and post-irradiation intergranular stress corrosion cracking behavior in high-purity 316 stainless steels, *J. Nucl. Mater.* 321 (2003) 192–209. [https://doi.org/10.1016/S0022-3115\(03\)00243-5](https://doi.org/10.1016/S0022-3115(03)00243-5).
- [48] W. Kuang, X. Feng, D. Du, M. Song, M. Wang, G.S. Was, A high-resolution characterization of irradiation-assisted stress corrosion cracking of proton-irradiated 316L stainless steel in simulated pressurized water reactor primary water, *Corros. Sci.* 199 (2022) 110187. <https://doi.org/10.1016/j.corsci.2022.110187>.
- [49] G.F. Li, Y.F. Kaneshima, T. Shoji, Effects of impurities on environmentally assisted crack growth of solution-annealed austenitic steels in primary water at 325°C, *Corrosion*. 56 (2000) 460–469. <https://doi.org/10.5006/1.3280550>.
- [50] P.L. Andreson, M.M. Morra, Effects of Si on SCC of Irradiated and Unirradiated Stainless Steels and Nickel Alloys, in: *NACE Corros. 2005*, Houston, TX, USA, 2005: pp. 1–27.
- [51] L. Tan, J.T. Busby, Formulating the strength factor α for improved predictability of radiation hardening, *J. Nucl. Mater.* 465 (2015) 724–730.
<https://doi.org/10.1016/j.jnucmat.2015.07.009>.
- [52] M.C. Hash, J.T. Busby, G.S. Was, The Effect of Hardening Source in Proton Irradiation-Assisted Stress Corrosion Cracking of Cold Worked Type 304 Stainless Steel, in: *Eff. Radiat. Mater. 21st Int. Symp.*, ASTM International, 2004: pp. 92–104.
- [53] P.L. Andresen, P.H. Chou, M.M. Morra, J. Lawrence Nelson, R.B. Rebak, Microstructural and stress corrosion cracking characteristics of austenitic stainless steels containing silicon, *Metall. Mater. Trans. A Phys. Metall. Mater. Sci.* 40 (2009) 2824–2836.
<https://doi.org/10.1007/s11661-009-9960-8>.
- [54] P.L. Andresen, C.L. Briant, Environmentally assisted cracking of types

- 304L/316L/316NG stainless steel in 288°C water, *Corrosion*. 45 (1989) 448–463.
<https://doi.org/10.5006/1.3582044>.
- [55] P.L. Andresen, C.L. Briant, Role of sulfur, phosphorus and nitrogen segregation on intergranular environmental cracking of stainless steels in high temperature water, *Proc. Third Int. Symp. Environmental Degrad. Materails Nulcear Power Syst. - Water React.* (1987) 371–381.
- [56] P.C. Wo, A.H.W. Ngan, Investigation of slip transmission behavior across grain boundaries in polycrystalline Ni₃Al using nanoindentation, *J. Mater. Res.* 19 (2004) 189–201. <https://doi.org/10.1557/jmr.2004.19.1.189>.
- [57] T.B. Britton, D. Randman, A.J. Wilkinson, Nanoindentation study of slip transfer phenomenon at grain boundaries, *J. Mater. Res.* 24 (2009) 607–615.
<https://doi.org/10.1557/jmr.2009.0088>.
- [58] Y. Guo, T.B. Britton, A.J. Wilkinson, Slip band-grain boundary interactions in commercial-purity titanium, *Acta Mater.* 76 (2014) 1–12.
<https://doi.org/10.1016/j.actamat.2014.05.015>.
- [59] J. Kacher, G.S. Liu, I.M. Robertson, In situ and tomographic observations of defect free channel formation in ion irradiated stainless steels, *Micron*. 43 (2012) 1099–1107.
<https://doi.org/10.1016/j.micron.2012.01.017>.
- [60] G.S. Was, Z. Jiao, J.T. Busby, Contribution of localized deformation to IGSCC and IASCC in austenitic stainless steels, *Fract. Nano Eng. Mater. Struct. - Proc. 16th Eur. Conf. Fract.* (2006) 677–678. https://doi.org/10.1007/1-4020-4972-2_335.
- [61] J. V. Sharp, Deformation of neutron-irradiated copper single crystals, *Philos. Mag.* 16 (1967) 77–96. <https://doi.org/10.1080/14786436708229258>.
- [62] P.L. Andresen, F.P. Ford, Fundamental modeling of environmental cracking for improved design and lifetime evaluation in BWRs, *Int. J. Press. Vessel. Pip.* 59 (1994) 61–70.
[https://doi.org/10.1016/0308-0161\(94\)90142-2](https://doi.org/10.1016/0308-0161(94)90142-2).
- [63] E.H. Lee, T.S. Byun, J.D. Hunn, M.H. Yoo, K. Farrell, L.K. Mansur, On the origin of deformation microstructures in austenitic stainless steel: Part I—Microstructures, *Acta Mater.* 49 (2001) 3269–3276.
- [64] T.S. Byun, E.H. Lee, J.D. Hunn, Plastic deformation in 316LN stainless steel - Characterization of deformation microstructures, *J. Nucl. Mater.* 321 (2003) 29–39.
[https://doi.org/10.1016/S0022-3115\(03\)00195-8](https://doi.org/10.1016/S0022-3115(03)00195-8).
- [65] T.S. Byun, N. Hashimoto, K. Farrell, Deformation mode map of irradiated 316 stainless steel in true stress-dose space, *J. Nucl. Mater.* 351 (2006) 303–315.
<https://doi.org/10.1016/j.jnucmat.2006.02.033>.
- [66] T.S. Byun, On the stress dependence of partial dislocation separation and deformation microstructure in austenitic stainless steels, *Acta Mater.* 51 (2003) 3063–3071.
[https://doi.org/10.1016/S1359-6454\(03\)00117-4](https://doi.org/10.1016/S1359-6454(03)00117-4).
- [67] E.H. Lee, T.S. Byun, J.D. Hunn, M.H. Yoo, K. Farrell, L.K. Mansur, On the origin of

- deformation microstructures in austenitic stainless steel: Part II - Mechanisms, *Acta Mater.* 49 (2001) 3277–3287. [https://doi.org/10.1016/S1359-6454\(01\)00193-8](https://doi.org/10.1016/S1359-6454(01)00193-8).
- [68] L. Wang, P. Guan, J. Teng, P. Liu, D. Chen, W. Xie, D. Kong, S. Zhang, T. Zhu, Z. Zhang, E. Ma, M. Chen, X. Han, New twinning route in face-centered cubic nanocrystalline metals, *Nat. Commun.* 8 (2017) 1–7. <https://doi.org/10.1038/s41467-017-02393-4>.
- [69] M.S. Wechsler, Dislocation Channeling in Irradiated and Quenched Metals, in: IS-2736; CONF-711047-1. Ames Lab., Ames, IA (United States), 1972.
- [70] M. Hiratani, H.M. Zbib, B.D. Wirth, Interaction of glissile dislocations with perfect and truncated stacking-fault tetrahedra in irradiated metals, *Philos. Mag. A Phys. Condens. Matter, Struct. Defects Mech. Prop.* 82 (2002) 2709–2735. <https://doi.org/10.1080/01418610208240062>.
- [71] M. Briceño, J. Fenske, M. Dadfarnia, P. Sofronis, I.M. Robertson, Effect of ion irradiation-produced defects on the mobility of dislocations in 304 stainless steel, *J. Nucl. Mater.* 409 (2011) 18–26. <https://doi.org/10.1016/j.jnucmat.2010.12.026>.
- [72] N.M. Ghoniem, S.H. Tong, B.N. Singh, L.Z. Sun, On dislocation interaction with radiation-induced defect clusters and plastic flow localization in fcc metals, *Philos. Mag. A Phys. Condens. Matter, Struct. Defects Mech. Prop.* 81 (2001) 2743–2764. <https://doi.org/10.1080/01418610108216667>.
- [73] A. Etienne, B. Radiguet, P. Pareige, Understanding silicon-rich phase precipitation under irradiation in austenitic stainless steels, *J. Nucl. Mater.* 406 (2010) 251–256. <https://doi.org/10.1016/j.jnucmat.2010.08.045>.
- [74] G.M. De Bellefon, J.C. Van Duysen, Tailoring plasticity of austenitic stainless steels for nuclear applications: Review of mechanisms controlling plasticity of austenitic steels below 400°C, *J. Nucl. Mater.* 475 (2016) 168–191. <https://doi.org/10.1016/j.jnucmat.2016.04.015>.
- [75] A. Etienne, B. Radiguet, P. Pareige, J.P. Massoud, C. Pokor, Tomographic atom probe characterization of the microstructure of a cold worked 316 austenitic stainless steel after neutron irradiation, *J. Nucl. Mater.* 382 (2008) 64–69. <https://doi.org/10.1016/j.jnucmat.2008.09.015>.
- [76] Z. Jiao, G.S. Was, Localized deformation and IASCC initiation in austenitic stainless steels, *J. Nucl. Mater.* 382 (2008) 203–209. <https://doi.org/10.1016/j.jnucmat.2008.08.032>.
- [77] T. Yonezawa, K. Suzuki, S. Ooki, A. Hashimoto, The effect of chemical composition and heat treatment conditions on stacking fault energy for Fe-Cr-Ni austenitic stainless steel, *Metall. Mater. Trans. A Phys. Metall. Mater. Sci.* 44 (2013) 5884–5896. <https://doi.org/10.1007/s11661-013-1943-0>.
- [78] M.J. Whelan, P.B. Hirsch, R.W. Home, W. Bollmann, Dislocations and stacking faults in stainless steel, *Proc. R. Soc. London. Ser. A. Math. Phys. Sci.* 240 (1957) 524–538.
- [79] M.J. Whelan, Dislocation interactions in face-centred cubic metals, with particular reference to stainless steel, *Proc. R. Soc. London. Ser. A. Math. Phys. Sci.* 249 (1959)

- 114–137. <https://doi.org/10.1098/rspa.1959.0011>.
- [80] K. Fukuya, S. Nakahigashi, S. Ozaki, S. Shima, Effects of phosphorus, silicon and sulphur on microstructural evolution in austenitic stainless steels during electron irradiation, *J. Nucl. Mater.* 179–181 (1991) 1057–1060. [https://doi.org/10.1016/0022-3115\(91\)90274-B](https://doi.org/10.1016/0022-3115(91)90274-B).
- [81] N. Shigenaka, T. Hashimoto, M. Fuse, Effects of alloying elements (Mo, Si) in an austenitic stainless steel on dislocation loop nucleation under ion irradiation, *J. Nucl. Mater.* 207 (1993) 46–52. [https://doi.org/10.1016/0022-3115\(93\)90246-U](https://doi.org/10.1016/0022-3115(93)90246-U).
- [82] S.I. Porollo, S. V. Shulepin, Y. V. Konobeev, F.A. Garner, Influence of silicon on swelling and microstructure in Russian austenitic stainless steel EI-847 irradiated to high neutron doses, *J. Nucl. Mater.* 378 (2008) 17–24. <https://doi.org/10.1016/j.jnucmat.2008.03.027>.
- [83] D. Chen, K. Murakami, K. Dohi, K. Nishida, N. Soneda, Z. Li, L. Liu, N. Sekimura, Radiation defects formed in ion-irradiated 316L stainless steel model alloys with different Si additions, *Mater. Trans.* 56 (2015) 1549–1552. <https://doi.org/10.2320/matertrans.MAW201503>.
- [84] G. Meric de Bellefon, K.M. Bertsch, M.R. Chancey, Y.Q. Wang, D.J. Thoma, Influence of solidification structures on radiation-induced swelling in an additively-manufactured austenitic stainless steel, *J. Nucl. Mater.* 523 (2019) 291–298. <https://doi.org/10.1016/j.jnucmat.2019.06.012>.